Delft University of Technology

Aerospace Engineering Faculty

Aerospace Structures & Materials Track

A continuum damage mechanics model for woven composites

Author:
Carlos Gámir Huguet

Supervisors:
Sonell Shroff, Claudio S. Lopes

A thesis submitted in partial fulfillment of the requirements for the degree of Master of Science in Aerospace Engineering

July 24, 2017

Abstract

A novel continuum damage mechanics model for 2D woven fabrics has been developed and implemented in a VUMAT subroutine for Abaqus/Explicit. The model takes into account the shear nonlinearity, the toughening mechanisms associated to tensile failure, and the influence of shear stresses in the initiation and propagation of tensile damage.

The non-linear shear behavior is reproduced by means of a Ramberg-Osgood equation. Permanent deformation, and the degradation of the secant shear modulus associated to the accumulation of matrix damage have been coupled to the formulation of this unidimensional plasticity law. The physical reference required to define completely the shear constitutive response proposed can be obtained from the experimental tensile test of ± 45 off-axis coupons. Failure initiation in tension is identified using Hashin's quadratic failure criterion, which accounts for the interaction of shear stresses in the promotion of tensile failure. A bilinear softening relation was selected to represent the combination of fibre breakage and toughening mechanisms characteristic of the intralaminar tensile fracture of these materials. Effort was placed on the development of a procedure for calibrating the softening relation associated to this failure mode. Specifically, this work addresses the applicability of linking the definition of a bilinear tensile damage law in homogenized continuum damage mechanics models for woven composites to the shape of a crack growth resistance curve measured with compact tension tests.

The constitutive model was validated including it in a set of finite element models of unnotched and open hole coupons with different multistacking sequences, under quasi-static tensile loading conditions, and comparing the results obtained by the simulation of the coupons against an experimental benchmark. A good correlation was achieved between the ultimate strength predicted with finite element analysis and the experimental data.

Keywords: Woven Composites, Finite Element Analysis, Continuum Damage Mechanics

Contents

List of Figures

List of Tables

List of Abbreviations

CC Compliance Calibration.

CDM Continuum Damage Mechanics.

CMOD Crack Mouth Opening Displacement.

CT Compact Tension.

DCB Double Cantilever Beam.

DIC Digital Image Correlation.

ENF End Notch Flexure.

ERR Energy Release Rate.

FE Finite Element.

NCAMP National Center for Advanced Materials Performance.

OHT Open Hole Tension.

R-curve Crack growth resistance curve.

UD Unidirectional.

UNT Unnotched Tension.

1 Introduction

Woven composites offer a good combination of damage tolerance, specific stiffness, and specific strength. However, when compared to unidirectional (UD) laminates with an equivalent volume fraction of in-plane fibres in all orientations, they present a lower in-plane stiffness and strength due to the tow waviness. In turn, woven composites are less vulnerable to delaminations and typically display a superior impact response. Additionally, due to their textile nature, they offer a higher drapability during manufacturing [14, 40]. For these reasons, the application of woven composites in the aeronautical, naval, and automotive industry is becoming increasingly widespread, especially in crash relevant parts [12].

Finite element (FE) analysis is commonly used to support the design and certification process of composite structures. The definition of a material model for 2D woven laminates capable of reproducing the effect of damage onset and propagation, could help to progress towards reducing the number of physical tests performed in the industry, hence resulting in cost savings and lower product design lead times.

There are multiple approaches to model damage in composites. The scope of this work is, however, limited to modeling intralaminar damage at macroscopic level based on continuum damage mechanics (CDM). With this approach, the failure mechanisms cannot be reproduced with the same level of detail than with micro/meso level models. However, macro-level analyses have proven to be by far more practical due to their relative simplicity and low computational cost, which makes them ideal for large scale simulations [29].

Most of the continuum damage models in the literature have been developed for unidirectional lamina composites. These models cannot be directly extrapolated to woven fabrics without considering the differences imposed by their dissimilar morphology. The existing material models for woven composites reported in the literature lag behind with respect to their UD counterparts in terms of complexity and overall development.

1.1 Aim

The aim of this thesis is to develop a homogenized continuum damage model for 2D carbon/epoxy woven fabrics capable of providing a good representation of intralaminar damage in unnotched and open hole coupons under tension.

1.2 Context

The project is the first part of a larger initiative seeking to develop a material model for predicting the ultimate strength of woven composite structures in a variety of loading situations, including not only tension but also compression and impact. This project has been carried out at IMDEA Materials Institute, which has provided the material and testing facilities necessary for its completion. The material system that has been used for the validation of the model is a carbon/epoxy preimpregnated AS4-8552-AGP193 plain weave fabric. The constitutive model presented has been included in a VUMAT user subroutine for Abaqus/Explicit.

1.3 Strategy & outline of the report

The document is organized as follows: First, in Section 2, a review is presented of the existing work concerning modeling the constitutive behavior in tension and shear prior and after failure initiation of woven fabrics with the CDM approach. After identifying the shortcomings of state-of-the-art material models, a novel CDM model is proposed. The description of the model is detailed in Section 3. Section 4 depicts the experimental work and simulations that have been carried out to obtain the material properties necessary for performing the validation. The constitutive model has been validated including it in a set of FE models of unnotched and open hole coupons, and comparing the ultimate strength predicted by the simulations against experimental results. This comparison is presented in Section 5 along with a discussion of the agreement obtained. Finally, in Section 6 conclusions are drawn about the work performed, and a set of recommendations for future developments of the material model are suggested.

2 State of the Art

2.1 Introduction

In 2D woven composites, the mechanical performance depends to a great extent on the interlacing pattern of the tows forming the plies (or fabrics). Commonly used weave styles include: plain, twill, basket and satin. Tows aligned in the main loading direction are referred to as warp, whereas the tows perpendicular to these are known as weft (see Figure 1) [20] .

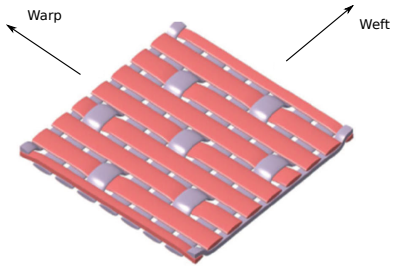

Figure 1: Schematic woven fabric [34].

Macroscale CDM models avoid modeling the weave architecture. Instead, they consider the fabric to be a continuum with homogenized orthotropic properties. Failure criteria are used to predict the onset of damage in the plies and determine which failure modes are involved in the initiation of failure. The accumulation of damage in the material volume is represented defining thermodynamically consistent internal damage variables that degrade the material stiffness matrix according to the failure modes triggered [17].

The most relevant characteristics of CDM models when it comes to predicting intralaminar damage in unnotched and open hole coupons in tension are the failure criteria, and the constitutive behavior in tension and shear prior and post failure initiation. This section addresses how these *"key"* characteristics are defined in state-of-the-art macroscale CDM models for woven composites in the interest of identifying the specific aspects that can be improved.

Section 2.2 reviews the selection of failure criteria for woven composites in macroscale damage models. The definition of the constitutive behavior in tension is examined in Section 2.3, followed by the definition of the shear constitutive behavior, in Section 2.4.

2.2 Failure criteria for woven fabrics

In models for progressive damage analysis for UD composites, it is a common practice for determining the onset of damage to use failure criteria distinguishing fibre failure modes and interfibre failure modes. Examples of these criteria are Puck [49] and LaRC [15]. The aforementioned criteria were developed for UD plies, and they are not applicable for woven fabrics because in these the transverse direction (weft) is fibre reinforced. As a result, the scarce macroscale damage models for woven fabrics usually adopt Maximum Stress criterion [13, 28, 40, 42], and consider the following failure modes: warp fibre tension, warp fibre compression, weft fibre tension, weft fibre compression and shear matrix cracking.

Cousigné et al. [13] evaluated the suitability of selecting Maximum Stress criterion for modeling intralaminar damage in woven fabrics. They developed a material model for LS-DYNA for woven composite materials accounting for permanent deformation and damage, and predicted ultimate failure of plain coupons in tension using either Maximum Stress or Tsai-Wu failure criterion [35]. It was concluded that the use of a non-interactive criterion (like Maximum Stress) leads to the overprediction of the strength of laminates with multidirectional stacking sequences. For these laminates, a good agreement with the experimental results was obtained using Tsai-Wu quadratic criterion.

The work performed by Cousigné et al. [13] revealed the need for more developed failure criteria for woven fabrics, taking into account the interaction between shear and tension failure modes. Tsai-Wu formulation

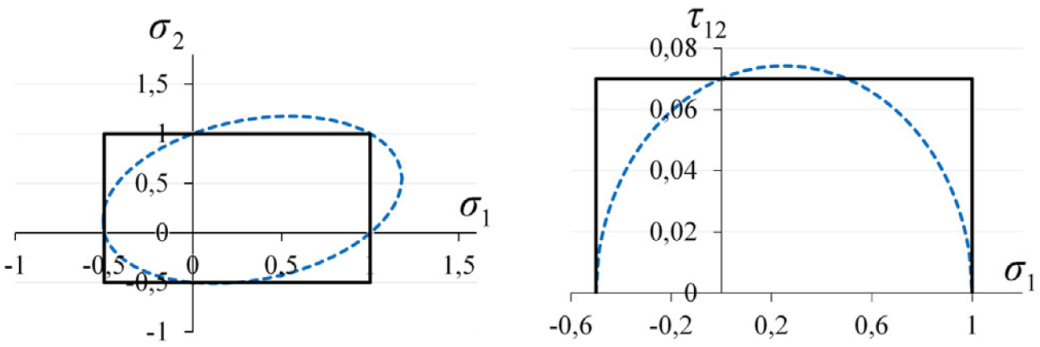

Figure 2: Schematic comparison of in-plane Tsai-Wu and Maximum Stress criteria [13]

is not a suitable criterion for CDM models. Firstly, because polynomial failure criteria (which also include Tsai-Hill, Azzi-Tsai, Hoffman etc. [47]) do not distinguish the modes responsible for failure. Thus, it is unclear how the elastic properties should be reduced after failure initiation. Secondly and more important, polynomial failure criteria are unphysical. For example in Tsai-Wu, the strength in a pure tension situation is affected by the uniaxial compressive strength allowable. The development of a failure criterion for woven composites that considers the interaction between failure modes should be based in the examination of the damage mechanisms associated to these modes.

The damage mechanisms in woven composites under tensile loading have been extensively studied in the literature through fractography analysis. Most authors agree that the sequence of events leading to failure of $[0]_n$ woven laminates under tension aligned in the warp direction is the following [20, 34]:

(i) Fibre-matrix debonding and matrix cracking in the weft tows.

(ii) Failure of the warp tows due to fibre breakage.

Greenhalgh [20] reported that, under warp tensile loading, the matrix damage at the weft tows generated in the early stages of the failure sequence indicated above act as initiation sites for fibre breakage in the warp tows. Figure 3 illustrate how the fracture planes in adjacent warp and weft tows are coincident, which is consistent with matrix damage in the weft tows having initiated the failure of the warp tows.

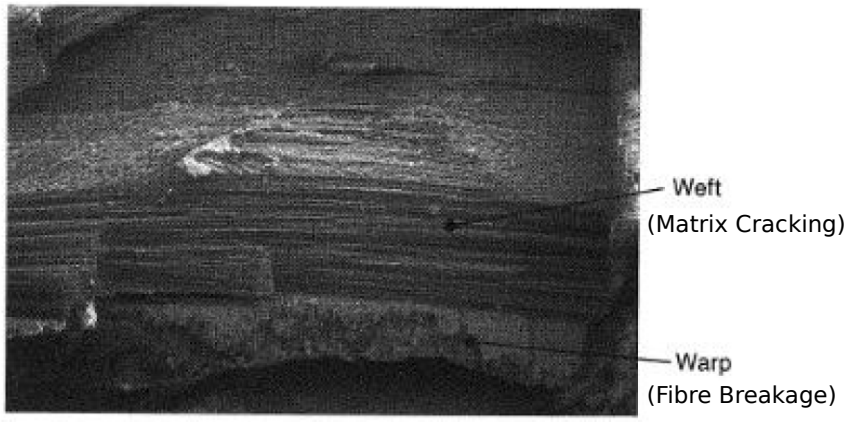

Figure 3: Fracture of a woven carbon/epoxy laminate in tension (x20) [20].

Lisle et al. [34] studied the damage mechanisms of woven composites under shear stress. They carried out $[\pm 45]_n$ off-axis tensile tests and observed the damage using infrared thermography and micrographic

cuts. It was concluded that damage caused by shear stresses primarily takes the form of matrix microcracks parallel to the fibres in both the warp and weft tows.

Figure 4 illustrates how the matrix damage in the material caused by tension and shear loading is distributed according to the observations from Greenhalgh [20] and Lisle et al. [34]. It can be noticed that the nature of the matrix damage caused by shear loading is the same than the damage acting as initiation site in tension. It is then logical to postulate that shear stresses prompt tensile failure at a strength lower than the uniaxial strength allowable. This may explain why Cousigné et al. [13] obtained a better agreement with the experimental results using Tsai-Wu failure criterion, which is stress-component interactive.

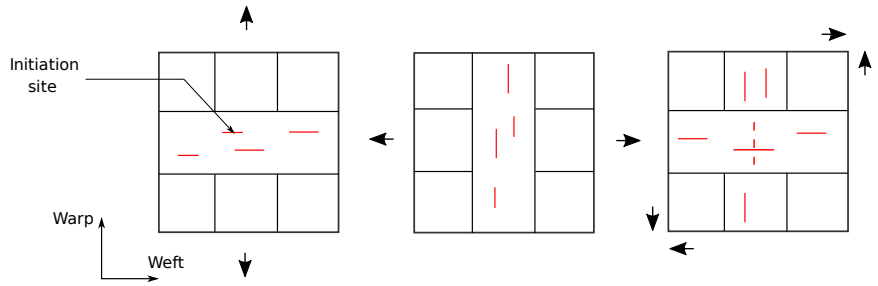

Figure 4: Scheme of the distribution of matrix damage for different loading situations based in the observations from Greenhalgh [20] and Lisle et al. [34].

Tsai-Wu failure criterion also assumes the interaction between longitudinal and transverse stresses in the initiation of failure (see Figure 2). The validity of this assumption for woven composites must however be brought into question. Tensile loading in the weft direction leads to matrix damage parallel to the fibres in the warp tows (see Figure 4). The effect that this type of damage may have in the promotion of warp tensile failure is expected to be much less pronounced than the generation of initiation sites, which are perpendicular to the fibres of the warp tows. On this subject, Welsh et al. [57] performed an experimental study of the biaxial behavior of glass fabric reinforced composites using cruciform specimens. They reported a square bounded failure surface $\sigma_{11} - \sigma_{22}$. Therefore, the biaxial interaction effect included in Tsai-Wu failure criterion (see Figure 2) is not supported by the experimental data, and should not be included.

Transverse and shear loading may have an effect in the warp compression failure mode. Some authors have suggested that, depending on the sign of the stress, transverse and shear loading could promote or prevent the formation of kink bands, the main damage mechanism in compression loading [40, 50]. This interaction is however out-of-the scope of this work, and should be the subject of future research.

2.3 Tensile constitutive behavior

Under tensile loads aligned in the warp or weft directions, the response of carbon/epoxy fabrics is linear elastic until the initiation of failure [13, 26, 34].

In Figure 5, a schematic constitutive response associated to tensile loading is depicted. In CDM models, when tensile failure is predicted by the failure criterion, the elastic modulus associated to the corresponding failure mode is degraded. Failure initiation is the state for which the material transitions from an elastic response to softening. The shape of the constitutive response during softening is known as damage law, and the state for which the stiffness is completely degraded is referred to as failure propagation [39]. During softening, fracture energy is dissipated. The total fracture energy dissipated when failure propagation is reached should be consistent with the crack propagation critical energy release rate (ERR), which is a property intrinsic of the material. This must be ensured in the numerical model regardless of the element size. For this purpose, in the formulation of the damage law the fracture energy should be regularized with the characteristic element length [5].

The damage law should be defined such that the softening behavior in the material is accurately represented. For this purpose, the selection of a suitable shape of the damage law associated to tensile failure

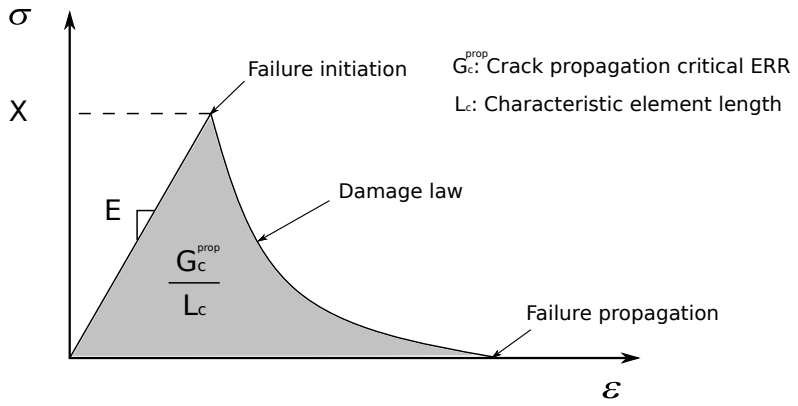

Figure 5: Schematic tensile constitutive response

should be based in the characterization of mode I intralaminar fracture.

In woven composites, the initiation of a mode I intralaminar crack starts with the brittle failure of the fibres. The initiation of the crack is followed by the formation of a damage zone behind the crack tip, wherein two toughening mechanisms take place simultaneously: fibre bridging and fibre pull-out (see Figure 6). The presence of these two mechanisms increment the resistance to crack propagation. As the crack propagates, the damage zone behind the crack tip grows, and thereby the effect of the two toughening mechanisms increase [8, 40].

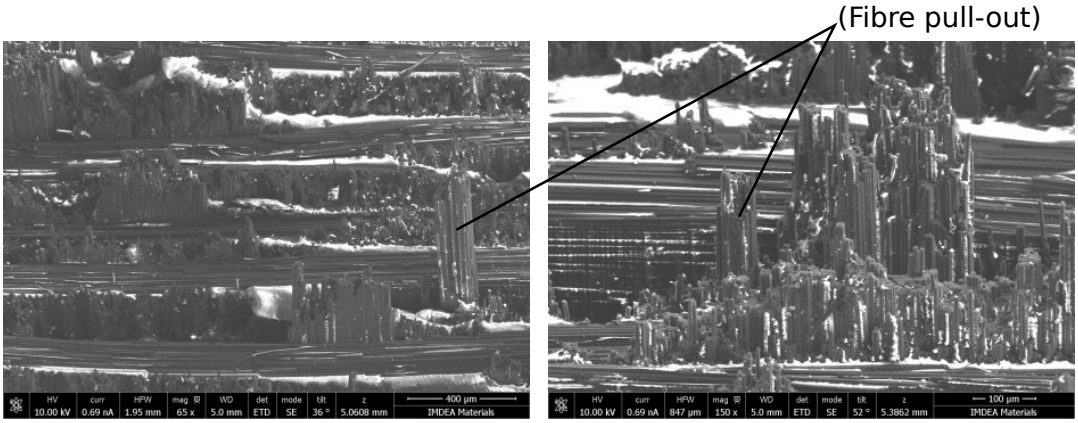

Figure 6: Scanning electron microscope images of the fracture surface of a carbon/epoxy woven composite loaded in tension [41].

This type of fracture process can be reproduced at the constitutive level with a damage law that begins with a sharp stiffness degradation and ends with a more gradual softening [16].

Martín-Santos et al. [40] reviewed the adequacy of a linear and a bilinear softening shape for predicting tensile failure in woven fabric composites. They proposed a macroscale CDM model for woven fabrics, and validated it by comparing the results of FE predictions with experimental data from open hole specimens with different widths, under tensile loading conditions.

With the linear damage law, although a good prediction of the ultimate strength of the wider specimens was achieved, the strength of the narrower specimens was overpredicted. This was attributed to the fact that in a narrow specimen, the distance between the hole and the edge of the coupon is small. Due to this,

a complete damage zone is not created before the ultimate strength of the coupon is reached. Consequently, the prediction of the ultimate strength mainly depends on the slope of the damage law right after failure initiation. With the linear damage law, the fracture energy is dissipated at the same rate from failure initiation until propagation. In comparison with the softening that would be needed to reproduce the fracture process characterized above, this results in an excessively gradual stiffness degradation right after failure initiation, hence the overprediction of the ultimate strength of the narrower coupons.

On the other hand, a good correlation with the experimental data was reported for all the specimen widths using a bilinear damage law (see Figure 7). These results reveal that the shape of the bilinear damage law is suitable for reproducing the abrupt stiffness drop associated to the fibre breakage taking place after failure initiation, and the transition to a tougher response corresponding to the bridging and pullout of the fibres [40].

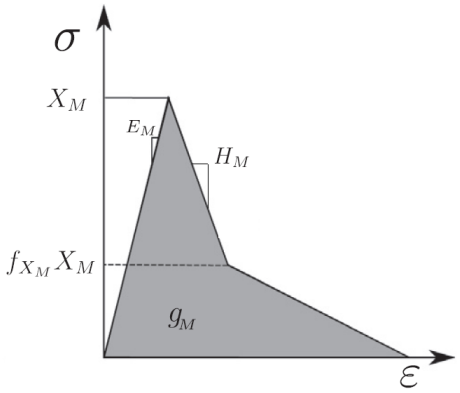

Figure 7: Scheme of the bilinear damage law proposed by Martín-Santos et al. [40].

In the bilinear damage law proposed by Martín-Santos et al. [40], the shape of the law is defined by two constants: the slope of the first part of the softening, and the stress at which the tougher phase begins (symbols H_M and $f_{Xm}X_M$ indicated in Figure 7). These two constants were calibrated by matching the prediction of the tensile strength of the open hole coupons to the experimental data. For calibrating the slope of the first part of the softening the authors used the narrower specimens, whilst for the calibration of the stress at which the tougher phase begins they used the wider specimens. This is not a valid methodology for the definition of the bilinear damage law, since basically the results of the open hole coupons, which were meant to be for validation, are being used for the calibration of the input.

To recapitulate, the work performed by Martín-Santos et al. points out that the bilinear damage law has a suitable shape for describing the tensile fracture process of woven composites. Nonetheless, it is necessary to develop a valid methodology for calibrating the law, preferably based on the characterization of the fracture process.

The fracture behavior of composites in tension is commonly characterized by the resistance curve. The resistance curve (or R-curve) is the evolution of the critical ERR with the crack growth [16]. The R-curve is commonly obtained from Compact Tension (CT) tests. Most of the work in this area derive from the CT standard test procedure for metals ASTM E399 [2]. There is little consensus as to how the specimen geometry should be defined to reduce unwanted failure mechanisms and produce representative resistance curves [7]. Over the years, several modified specimen geometries have been suggested. Perhaps the most widespread is the one proposed by Pinho [48] for UD composites, depicted in Figure 8. Its use has been later extended to textile composites. To cite an example, García-Carpintero et al. [19] measured the resistance curve of a triaxial braided composite using this test procedure.

To the author's knowledge, no CDM macroscale model for woven composites has been proposed in which the tensile damage law is defined based on the resistance curve. This approach has however been achieved for UD composites.

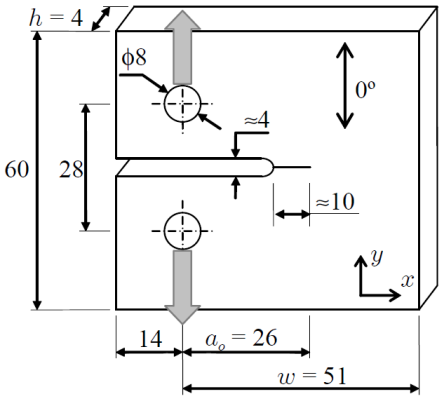

Figure 8: Compact tension specimen geometry proposed by Pinho [48] .

Davila [16] studied the relationship between the resistance curve and the shape of a traction/displacement softening law for UD composites. He developed a procedure in which the crack opening is modeled using two superimposed cohesive elements. Each cohesive element represents one aspect of the fracture process: the fibre breakage, and the toughening mechanisms. Figure 9a presents the superposition of the softening laws corresponding to the cohesive elements. The cohesive element associated to the fracture of the fibres has a softening law with a high strength and a brittle failure, whereas the softening law of the cohesive element associated to the fibre bridging and pull-out mechanisms has a low strength and a tough failure.

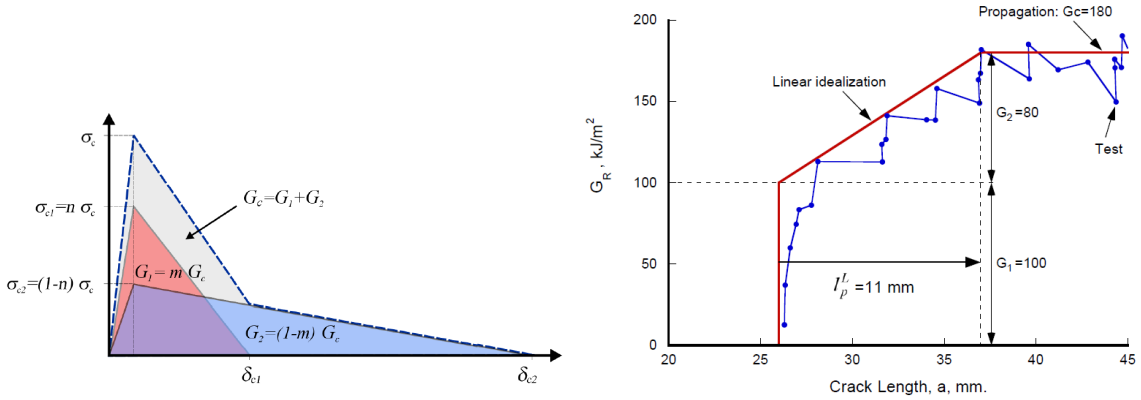

(a) Combination of two superposing softening laws. (b) Resistance curve obtained from Pinho's CT test.

Figure 9: Softening law obtained by superposition of two cohesive elements proposed by Davila [16].

The strength and the crack propagation critical ERR of the softening law associated to each cohesive element was formulated as a function of the shape of the resistance curve. The resistance curve— included in Figure 9b— was obtained using Pinho's compact tension test data. Davila [16] proposed to linear idealize the resistance curve in order to ease its relation with the softening laws. The shape of the resistance curve could then be defined by only three parameters: the crack initiation critical ERR, the crack propagation critical ERR, and the length of the process zone [1]. The crack initiation critical ERR identified in the resistance curve was attributed to the fracture toughness of the brittle softening law, and the difference between the initiation and propagation critical ERR's was associated to the fracture toughness of the softening law representing the effect of the toughening mechanisms.

[1]These properties are indicated with the symbols G_1, G_c and l_p^L respectively in Figures 9b and 9a. However, this notation will not be followed in the present work.

This procedure was validated comparing the response predicted by a shell FE model of the compact tension test— including the superposed cohesive elements— against the data from the experimental test. An excellent agreement was found.

Modeling intralaminar failure with cohesive elements is not the approach proposed in this work. However, the methodology proposed by Davila [16] seems to be a convenient way of including the information about the fracture processes responsible for mode I intralaminar crack opening in the definition of a bilinear tensile damage law. To that end, it would be needed to adapt the formulation for cohesive elements to a format compatible with the CDM based approach. Also, since the work performed by Davila is focused towards UD composites the applicability of the same methodology for woven composites must be examined.

2.4 In-plane shear constitutive behavior

Under in-plane shear loading, woven fabrics display a highly non-linear constitutive behavior. The non-linearity is caused by a combination of matrix microplasticity, microcracking, and fibre rotation, which take place at different stages of deformation [34].

Hufner [27] identified these stages in the off-axis response of a $[\pm 45]_n$ glass reinforced woven laminate in tension. He divided the response in four zones (see Figure 10). For low strains, the response is nearly elastic (zone 1). Larger strains cause matrix microcracking and microplasticity, which decrease the shear modulus of the material (zone 2). For even larger strains, the initiation and propagation of microcracks is slowed down due to crack saturation. At the same time, warp and weft fibre bundles tend to align with the load direction. This phenomenon is referred to as trellising (or trellis effect). During this region, the curve is again linear (zone 3). The material ends up failing at a very high strain level due to the breakage of the fibres in tension (zone 4).

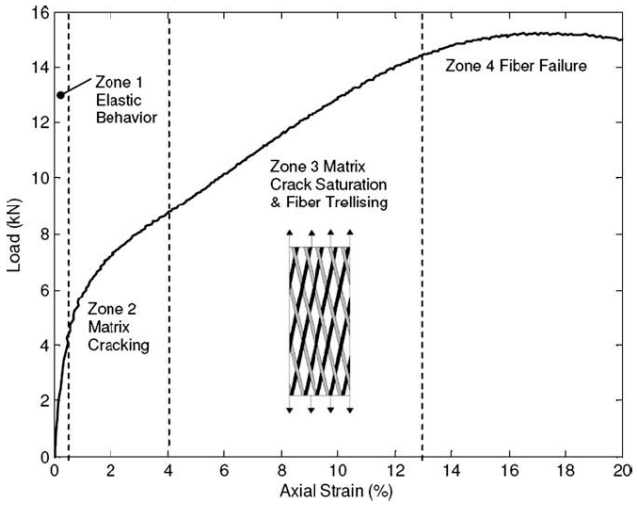

Figure 10: Typical off-axis response of a $[\pm 45]_n$ woven laminate [27]

.

CDM models for woven composites commonly include the non-linear shear behavior corresponding to the zones 1 and 2 adopting a unidimensional plasticity formulation [13,40], which are functions relating the shear stress component to the shear strain. To a greater or lesser extent, unidimensional plasticity formulations are calibrated using experimental data. Over the years, a large number of these expressions have been proposed. The most known are maybe the ones proposed by Hahn-Tsai [22], Sun-Chen [52] and Ogihara [46]. Rose [51] signaled that at least two fitting parameters are needed to closely match the experimental shear response of UD composites. He pointed out that Ramberg-Osgood equation can provide a better approximation than Hahn-Tsai. Figure 11 compares the flexibility of Hahn-Tsai and Ramberg-Osgood equation for fitting

experimental shear data from the World Wide Failure Exercise. In this line, the use of Ramberg-Osgood equation for fitting the in-plane shear response of woven fabrics has been recommended by Cox [14]. Off-axis tensile tests can be used to obtain the physical reference necessary for the calibration.

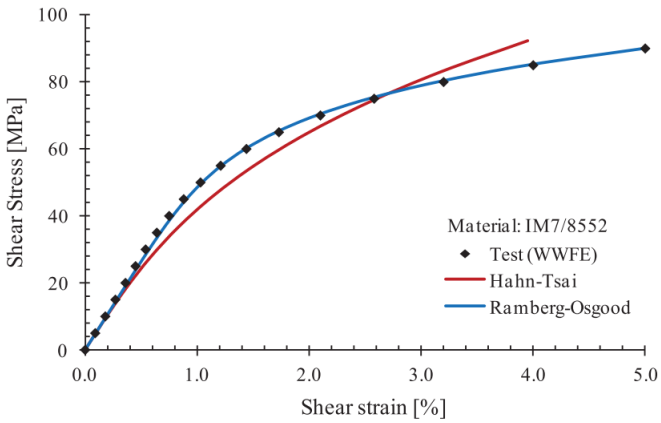

Figure 11: Comparison of the flexibility of Hahn-Tsai and Ramberg-Osgood equation [51].

.

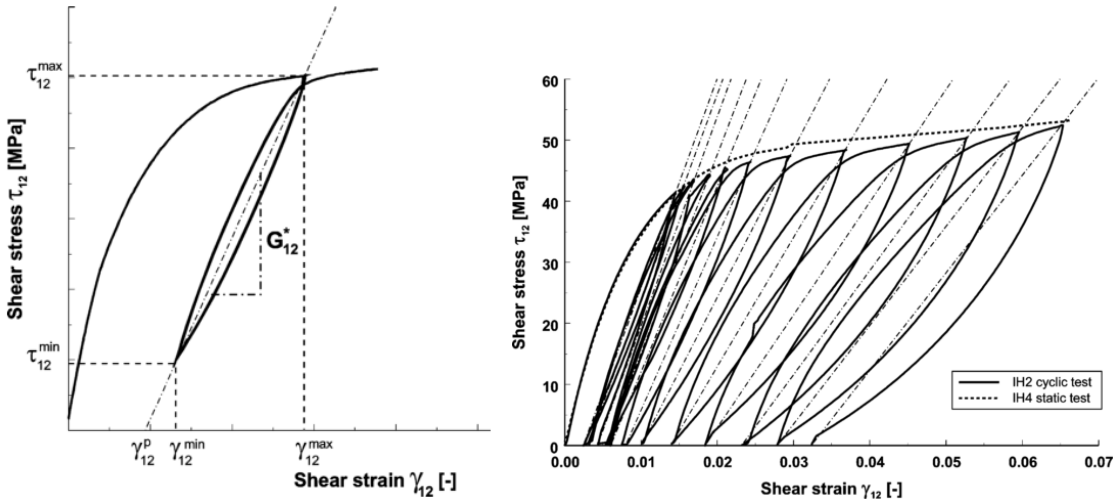

(a) Definition of the secant shear modulus G^*_{12}. (b) Evolution of the secant modulus with the shear strain.

Figure 12: Cyclic in-plane shear loading of a $[\pm 45°]_{2s}$ UD glass/epoxy laminate. [56]

In a shear constitutive model accounting for permanent deformation, the response of the material in unloading situations must be defined. This requires to quantify to which extent the generation of damage in the matrix is responsible for the shear non-linear behavior. Static in-plane shear tests— while convenient— do not provide any information exclusively about the extent of damage in the material. This results from the fact that plasticity and damage contribute conjointly to the non-linearity. Van Paepegem [56] proposed to decouple these two contributions using cyclic tensile tests of $[\pm 45]_n$ laminates (ASTM D 3518 [4]). In a cyclic tensile test, each cycle is characterized by the secant shear modulus G^*_{12}, defined as illustrated in Figure 12a. During unloading, only the elastic strain and the strain caused by the damage are recovered. In other words, the plastic strain γ_{12p} is permanent. As can be seen in Figure 12b, the secant shear modulus decreases with the strain. The explanation proposed by the author is that the portion of the strain associated to the damage

grows from cycle to cycle. The degradation of the secant shear modulus from its pristine state is therefore solely attributed to the accumulation of damage in the matrix. The description of the cycles proposed by Van Paepegem can be used for defining the unloading response in a CDM model. This approach was followed by Tan [53] in a material damage model for UD carbon/PEKK plies. Since the mechanisms causing the shear non-linear behavior in UD and woven plies are— at its core— the same, using the formulation developed by Van Paepegem for describing the unloading response of woven fabrics is a priori a suitable method.

Due to the trellis effect, it is not possible to obtain a physical reference of the shear constitutive behavior of woven fabrics for high strains (zone 3 and above in Figure 10). The stiffening caused by the rotation of the warp and weft fibre bundles should not be attributed to the shear constitutive response, but rather to the fact that the material is being increasingly loaded in tension [28]. State-of-the-art CDM models developed for UD and woven laminas including shear non-linearity typically neglect the fibre rotation and extend the unidimensional plasticity formulation to high shear strains [13, 40, 44, 53].

Macroscale material models for woven composites consider damage caused by shear loading to be a separate failure mode (see Section 2.2). Since it is not possible to obtain a physical reference exclusively of the shear softening, the definition of failure initiation and the post failure behavior in these models is not performed appropriately. In conventional laminates complying with the 10% design rule, plies at 0° and 90° fail before these stages of deformation are reached [28]. The definition of the constitutive behavior for high shear strains— including softening— is in principle irrelevant for the determination of the ultimate strength of unnotched and open hole coupons with multidirectional stacking sequences [40].

2.5 Conclusions

In this section, it has been addressed how the failure criterion and the constitutive behavior in tension and shear prior and post failure initiation should be defined in a macroscale CDM model for woven composites in order to obtain a good prediction of the intralaminar damage in unnotched and open hole coupons under tension. In the process, the specific aspects that can be improved in the state-of-the-art models reported in the literature have been highlighted.

Failure criteria for woven composites should be further developed. The formulation of such failure criteria should derive from the damage mechanisms involved in the failure modes and their interaction. It has been postulated, based in the analysis of fractography, that the matrix damage caused by shear loading promotes failure in tension at a strength lower than the uniaxial allowable. Also, it has also been signaled that there is not a significant interaction between the warp and weft tensile failure modes. The failure criterion of the CDM model should take into account these considerations.

Under tensile loading aligned in the warp or weft direction, the response prior to failure initiation of carbon/epoxy woven fabrics is linear elastic. After failure initiation, mode I intralaminar crack opening is characterized by a toughening effect. The bilinear damage law has a suitable shape for describing the increase of toughness caused by the pull-out and bridging of the fibres. The input determining the form of the bilinear damage law should be defined based on the resistance curve, which can be measured from compact tension tests. A procedure for defining the damage law based on the resistance curve has not been reported yet for woven composites. For establishing the relationship between the resistance curve and the damage law it has been proposed to adapt the formulation developed by Davila [16] for cohesive elements to a format compatible with the CDM approach.

The in-plane shear response of woven fabrics is characterized by being non-linear. This response can be fitted using a unidimensional plasticity formulation. Ramberg-Osgood equation is a suitable expression for this purpose. The experimental reference required to calibrate the function can be obtained from off-axis tensile tests of $[\pm 45]_n$ laminates. Finally, cyclic off-axis tensile tests can be used to measure the evolution of the secant shear modulus and the permanent deformation, with a view to defining the unloading shear response.

3 Description of the constitutive model

In what follows, the CDM based model proposed for woven fabrics is presented. The constitutive behavior in tension and shear has been defined based on the conclusions drawn from the survey depicted in the previous section. The response of the material under compression and out-of-plane loading— despite not being important for obtaining a good prediction of the tensile strength of the coupons— has been also included in the model.

The material model has been implemented in a VUMAT user subroutine for 3D elements for Abaqus Explicit. The input of the algorithm is the strain increment $\boldsymbol{\Delta\epsilon^t}$ and the strain from the previous time increment $\boldsymbol{\epsilon^{t-1}}$. Based on this, the code updates the strain $\boldsymbol{\epsilon^t}$ and computes the nominal stress $\boldsymbol{\sigma^t}$. Figure 13, presents the general structure of the constitutive model.

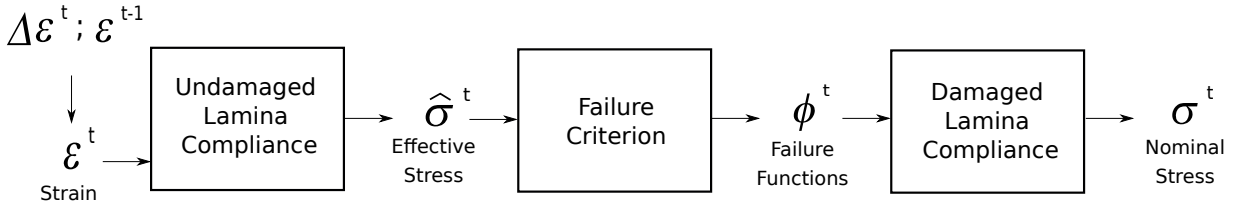

Figure 13: General structure of the constitutive model.

The stress in the absence of damage $\hat{\boldsymbol{\sigma}}^{\boldsymbol{t}}$, referred to as effective stress, is computed using the undamaged lamina compliance. This step is developed in Section 3.1. Subsequently, the effective stress state is evaluated using a failure criterion. Section 3.2 addresses the detection of failure initiation and the computation of the failure functions $\boldsymbol{\phi^t}$. After evaluating the effective stress, the compliance of the material is degraded and the nominal stress $\boldsymbol{\sigma^t}$ is computed. This is the final step, and it described in Section 3.3.

3.1 Computation of the effective stress tensor

The response of the fabric in the absence of damage is represented by a three-dimensional orthotropic constitutive relation. Given the existence of two symmetry planes, the extension to shear coupling of the compliance matrix is null. Because of this, the shear behavior can be treated separately. In tension and in compression aligned in the warp, weft and out-of-plane directions, a perfectly elastic response has been assumed. On this basis, the three principal effective stress components are computed from the compliance matrix depicted in the system 1. [2]

$$\begin{pmatrix}\epsilon_{11}\\ \epsilon_{22}\\ \epsilon_{33}\end{pmatrix} = \begin{pmatrix}\frac{1}{E_1} & -\frac{\nu_{12}}{E_1} & -\frac{\nu_{13}}{E_1}\\ -\frac{\nu_{12}}{E_1} & \frac{1}{E_2} & -\frac{\nu_{23}}{E_2}\\ -\frac{\nu_{13}}{E_1} & -\frac{\nu_{23}}{E_2} & \frac{1}{E_3}\end{pmatrix}\begin{pmatrix}\hat{\sigma_{11}}\\ \hat{\sigma_{22}}\\ \hat{\sigma_{33}}\end{pmatrix} \Rightarrow \begin{pmatrix}\hat{\sigma_{11}}\\ \hat{\sigma_{22}}\\ \hat{\sigma_{33}}\end{pmatrix} \tag{1}$$

The in-plane shear behavior is non-linear. Such response originates from the accumulation of damage and plasticity in the matrix [27]. In order to represent this effect, the Ramberg-Osgood formulation has been adopted. In particular, the equation 2 implemented in the model is a reformulation derived by Bogetti et

[2] In the interest of clarity, the superindex "t" indicating the time increment corresponding to the computation of the stress tensor has been ommited.

al. [9], in which the effective stress $\hat{\tau_{12}}$ is written explicitly in terms of the strain γ_{12}. The constants ρ and τ_{12}^{a} control the non-linearity of the constitutive relation.

$$\hat{\tau_{12}} = \frac{G_{12}\ \gamma_{12}}{\left(1 + \left(\frac{G_{12}\ |\gamma_{12}|}{\tau_{12}^{a}}\right)^{\rho}\right)^{1/\rho}} \tag{2}$$

In the proposed model for in-plane shear, the strain γ_{12} is considered to be composed by a recoverable part, and an inelastic (non-recoverable) part. The recoverable part comprises the elastic portion of the strain, and the one associated to the accumulation of damage, whilst the inelastic part, hereinafter referred to as γ_{12p}, includes the shear strain caused by the matrix plasticity. The equation presented in 2 is not valid for unloading situations. Instead, if unloading initiates at a given strain γ_{12}^{unl}, it is assumed to take place following a straight path defined by the secant shear modulus $G_{12}^{*}(\gamma_{12}^{unl})$. The equation 3, proposed by Van Paepegem et al. [56] has been used to describe the unloading path in this situation. Figure 14, provides a graphical representation of the shear constitutive model before failure initiation.

$$\hat{\tau_{12}} = G_{12}^{*}(\gamma_{12}^{unl})(\gamma_{12} - \gamma_{12p}(\gamma_{12}^{unl})) \qquad with \qquad \gamma_{12p}(\gamma_{12}) = \gamma_{12} - \frac{\hat{\tau_{12}}(\gamma_{12})}{G_{12}^{*}(\gamma_{12})} \tag{3}$$

If the stress level at which unloading began ($\hat{\tau_{12}}^{y}$ in Figure 14) is recovered, the equation 3 is abandoned to regain the non-linear path associated to equation 2.

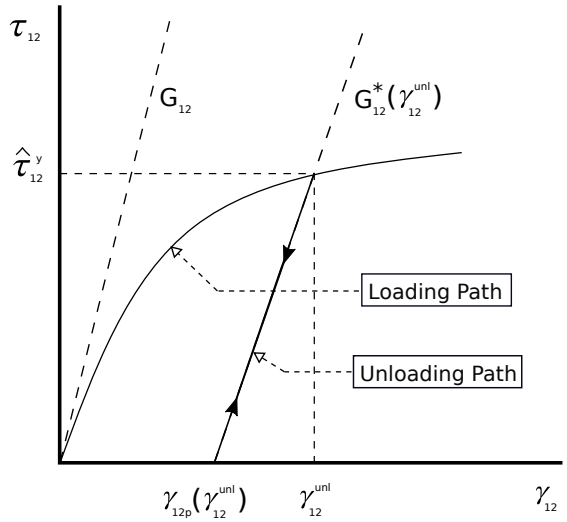

Figure 14: In-plane shear constitutive behavior before failure initiation.

For the out-of-plane shear (13) and (23) the same non-linear behavior that the one depicted for in-plane shear has been adopted. In the interest of brevity, the formulation of the effective stress components $\hat{\tau_{13}}$ and $\hat{\tau_{23}}$ has not been included.

3.2 Failure modes and detection of failure initiation

In this section, the criteria selected for determining failure initiation are presented. The CDM based model proposed considers the following in-plane failure modes: fibre failure in tension in the warp and weft directions; failure in compression in the warp and weft directions; and failure due to in-plane shear loading. The failure modes corresponding to out-of-plane perpendicular compression, out-of-plane shear (13) and out-of-plane shear (23), are of great importance in various types of simulations, such as impact. Due to this

and with a view to future developments, these modes have been included as well in the numerical model. Nonetheless, since they have no influence in the prediction of the strength of the coupons in tension, they are not relevant in this study. As such, the description of these failure modes is not developed in this document.

A failure function ϕ_i is defined for each i failure mode. Failure functions compare the effective stress state with an envelope of stress states associated to failure in a given mode. These envelopes are defined as a function of the uniaxial strength allowables. Table 1 lists the failure modes that will be considered and the nomenclature chosen to define their corresponding failure functions.

Failure Mode	i	Failure Criterion	Failure Function
Warp Tension	1+	Hashin	ϕ_{1+}
Warp Compression	1−	Max. Stress	ϕ_{1-}
Weft Tension	2+	Hashin	ϕ_{2+}
Weft Compression	2−	Max. Stress	ϕ_{2-}
Out-of-plane Compression	3	Max. Stress	ϕ_3
Out-of-plane Shear (13)	4	Max. Stress	ϕ_4
Out-of-plane Shear (23)	5	Max. Stress	ϕ_5
In-plane Shear (12)	6	Max. Stress	ϕ_6

Table 1: Failure modes and their corresponding failure criteria and failure functions.

As was seen in Section 2.2, in woven fabrics shear stresses generate matrix cracks that act as initiation sites for failure in tension. In order to incorporate this interaction, Hashin [23] quadratic failure criterion has been chosen. The criteria for tensile failure in the warp and weft directions are depicted in the equations 4 and 5, wherein X_T represents the tensile strength in the warp direction, Y_T the tensile strength in the weft direction, and S_L the in-plane shear strength. Two parameters α_1 and α_2 have been added to control the degree of influence of the effective in-plane shear stress $\hat{\tau_{12}}$ in the tensile strength.

$$\phi_{1+} = \left(\frac{\hat{\sigma_{11}}}{X_T}\right)^2 + \alpha_1 \left(\frac{\hat{\tau_{12}}}{S_L}\right)^2, \qquad \text{if } \hat{\sigma_{11}} \geq X_T^{min} \tag{4}$$

$$\phi_{2+} = \left(\frac{\hat{\sigma_{22}}}{Y_T}\right)^2 + \alpha_2 \left(\frac{\hat{\tau_{12}}}{S_L}\right)^2, \qquad \text{if } \hat{\sigma_{22}} \geq Y_T^{min} \tag{5}$$

There is no evidence or justification supporting that the tensile failure of the fibres affect the shear strength of the fabrics. Therefore, in-plane shear failure initiation is defined by the maximum stress criterion:

$$\phi_6 = \frac{|\hat{\tau_{12}}|}{S_L} \tag{6}$$

Figures 15a and 15b show the failure envelopes associated to the in-plane shear–tension interactive criterion. If no limit were added to the interaction, failure in tensile mode could be triggered exclusively due to a high effective shear stress $\hat{\tau_{12}}$. This would be unrealistic. To avoid this, a minimum effective stress for tensile failure denoted as X_T^{min} for the warp direction and Y_T^{min} for the weft direction has been included in the equations 4 and 5. These limits have been set to correspond with the points in the failure envelopes at which failure takes place simultaneously in tension and shear. Thus, the constants X_T^{min} and Y_T^{min} have been assigned to the effective stresses $\hat{\sigma_{11}}$ and $\hat{\sigma_{22}}$ computed at the intersection of equation 6 with the equations 4 and 5 respectively: [3]

$$X_T^{min} = \sqrt{1-\alpha_1}\; X_T \qquad Y_T^{min} = \sqrt{1-\alpha_2}\; Y_T \tag{7}$$

[3]For the case in which $0 < \hat{\sigma_{11}} < X_T^{min}$, the warp tensile failure function in the numerical model takes the form $\phi_{1+} = \hat{\sigma_{11}}/X_T$. However since $X_T^{min} < X_T$, this case can never predict failure initiation (see Figure 15a). The same applies for the tensile criterion associated to the weft direction.

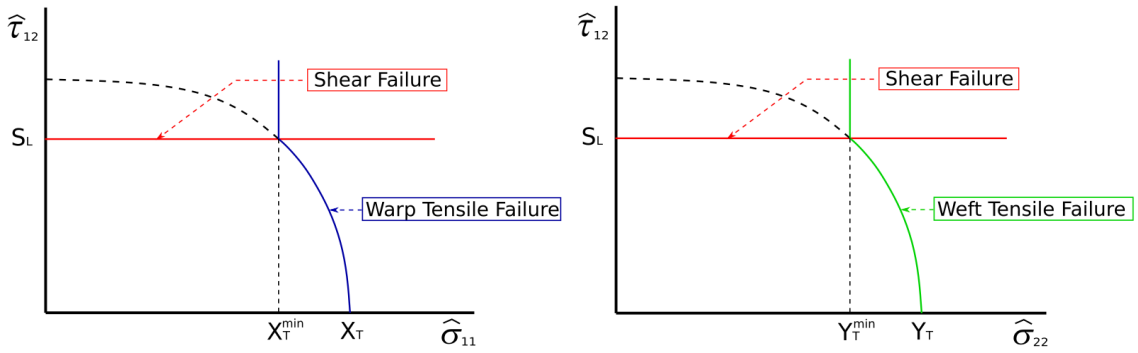

(a) Failure envelope $\tau_{\hat{12}} - \sigma_{\hat{11}}$.

(b) Failure envelope $\tau_{\hat{12}} - \sigma_{\hat{22}}$.

Figure 15: In-plane shear — tension interactive criterion

For the rest of failure modes, failure initiation is defined by the maximum stress criterion. The corresponding failure functions are indicated in equation 8, wherein X_C stands for the warp compressive strength, Y_C for the weft compressive strength, S_R for the out-of-plane shear strength, and Z_C for the out-of-plane compressive strength.

$$\phi_{1-} = \frac{|\hat{\sigma_{11}}|}{X_C} \qquad \phi_{2-} = \frac{|\hat{\sigma_{22}}|}{Y_C} \qquad \phi_3 = \frac{|\hat{\sigma_{33}}|}{Z_C} \qquad \phi_4 = \frac{|\hat{\tau_{13}}|}{S_R} \qquad \phi_5 = \frac{|\hat{\tau_{23}}|}{S_R} \tag{8}$$

3.3 Computation of the nominal stress tensor

3.3.1 Orthotropic damage model

The stiffness degradation scheme adopted is an adaptation of the one proposed by Maimi et al. [37,39] later used for woven fabrics by Muñoz et al. [42]. The scheme has been modified to include some consequences arising from having selected a non-linear formulation for in-plane and out-of-plane shear before failure initiation. Likewise in Section 3.1, the in-plane and out-of-plane shear constitutive behaviors are treated separately.

In the degradation scheme implemented, each modulus in the diagonal of the compliance matrix is affected by a damage variable d_i, evolving from from 0 (undamaged state) to 1 (fully damaged state). These variables are defined based on the failure functions ϕ_i presented in the previous section, which contain the information about by how much the effective stress has exceeded the strength. The compliance of the material, except for the shear constitutive relations, is presented in the following system of equations:

$$\begin{pmatrix} \epsilon_{11} \\ \epsilon_{22} \\ \epsilon_{33} \end{pmatrix} = \begin{pmatrix} \frac{1}{(1-d_1)E_1} & -\frac{\nu_{12}}{E_1} & -\frac{\nu_{13}}{E_1} \\ -\frac{\nu_{12}}{E_1} & \frac{1}{(1-d_2)E_2} & -\frac{\nu_{23}}{E_2} \\ -\frac{\nu_{13}}{E_1} & -\frac{\nu_{23}}{E_2} & \frac{1}{(1-d_3)E_3} \end{pmatrix} \begin{pmatrix} \sigma_{11} \\ \sigma_{22} \\ \sigma_{33} \end{pmatrix} \Rightarrow \begin{pmatrix} \sigma_{11} \\ \sigma_{22} \\ \sigma_{33} \end{pmatrix} \tag{9}$$

When defining the stiffness degradation associated to the in-plane shear mode, two major considerations should be taken into account:

(i) The energy dissipated during the generation of the inelastic strain before failure initiation is not associated to the fracture process.

(ii) The stiffness degradation during the softening part of the constitutive behavior starts from a pre-existent level caused by the accumulation of damage prior to failure initiation.

As a consequence of the first premise, it is not possible to provide a combined formulation for both the in-plane shear stress before failure initiation and after failure initiation likewise the other constitutive relations presented in the system of equations 9. The nominal stress τ_{12} during softening should be computed based in the portion of the strain corresponding to elasticity and damage, excluding the plastic strain at failure γ^0_{12p} [4]. Regarding the second premise enounced, the preexistence before failure initiation of damage is accounted by considering that the stiffness degraded after failure initiation is the secant modulus at failure initiation $G^*_{12}(\gamma^0_{12})$ instead of the pristine modulus G_{12}. This degradation is controlled by the damage variable associated to in-plane shear failure d_6.

All things considered, the nominal stress component τ_{12} is computed based in the following equation:

$$\tau_{12} = \begin{cases} \hat{\tau_{12}}, & \text{if } d_6 = 0 \\ G^*_{12}(\gamma^0_{12})\ (1 - d_6)\ (\gamma_{12} - \gamma^0_{12p}), & \text{otherwise} \end{cases} \tag{10}$$

Each damage variable d_i is defined as a function of an internal threshold variable $r_i(\phi_i)$. The threshold variable $r_i(\phi_i)$ store the information about the accumulation of damage in the failure mode i. The relation between the damage variable d_i and the threshold variable $r_i(\phi_i)$ is what was referred in Section 2.3 as damage law. Its definition is addressed in the next sections.

In particular, Section 3.3.2 focus on the definition of the damage laws corresponding to the failure modes associated to the warp direction. Section 3.3.3 concentrate on the definition of the damage law associated to in-plane shear. Since the damage laws associated to the weft direction have the same formulation than those corresponding to the warp direction, in the interest of brevity, they have been omitted. Similarly, given that the rest of failure modes are not relevant in this study, their definition is not presented in this document. [5]

3.3.2 Warp tension & compression damage laws

In the warp direction, there are two failure modes that can potentially affect the modulus E_1 of the first term of the compliance matrix: tensile failure and compressive failure. Each of them, has a damage variable associated: d_{1+} for tension, and d_{1-} for compression. Although two failure modes can be triggered by loading in the warp direction, only one damage variable d_1 affects the modulus E_1. Whether d_{1+} or d_{1-} corresponds to d_1 in the equation 9 is determined by the sign of the effective stress $\hat{\sigma_{11}}$, evaluated in the equation 11 [37], wherein $\langle\bullet\rangle$ is the McCauley operator defined as $\langle\bullet\rangle = (\bullet + |\bullet|)/2$.

$$d_1 = d_{1+}\frac{\langle\hat{\sigma_{11}}\rangle}{|\hat{\sigma_{11}}|} + d_{1-}\frac{\langle-\hat{\sigma_{11}}\rangle}{|\hat{\sigma_{11}}|} \tag{11}$$

The damage variables d_{1+} and d_{1-} are functions of the threshold variables r_{1+} and r_{1-} respectively. The threshold variables have been defined with the formulation proposed by Maimi et al. [37], indicated in the equations 12. These expressions meet the Kuhn-Tucker and consistency conditions necessary to ensure the non-reversibility of damage and the numerical stability of the model, and consider the coupling of the compression damage with the tension damage. Damage caused by compression loading affects the response of the material during tension loading, but —due to crack closure— not viceversa. [6]

$$r_{1+} = max\left(1, \phi_{1+}, r^{t-1}_{1+}, \phi_{1-}, r^{t-1}_{1-}\right) \qquad ; \qquad r_{1-} = max\left(1, \phi_{1-}, r^{t-1}_{1-}\right) \tag{12}$$

The response of the material in case of unloading and load reversal cycles after failure initiation is defined by the conditions expressed in the equations 11 and 12. The reader is referred to the work of Maimi et al. [37, 39], for further information in this regard.

[4] The superscript "0" indicates that the variable affected corresponds to the failure initiation point

[5] For the out-of-plane perpendicular compression, an exponential damage law with the formulation developed by Maimi et al. [37, 39] has been implemented in the numerical model. Regarding the out-of-plane shear modes, the same formulation than that for in-plane shear has been included.

[6] The superscript "t-1" indicates that the variable affected is the one computed in the previous increment.

3.3.2.1 Warp tensile damage law

A bilinear damage law has been implemented for the tensile mode. The proposed damage law $d_{1+}(r_{1+})$ is an adaptation of the formulation for cohesive elements developed by Davila [16] — reviewed in Section 2.3—, to a formulation compatible with the CDM based approach.

The definition of the damage law is directly related to the shape of a linear idealized crack growth resistance curve (R-curve). The R-curve is the evolution of the critical energy release rate G_{Ic} with the instantaneous crack length a. Figure 16a depicts the form that takes its linear idealization. Three parameters are needed to define the shape of the aforementioned curve: the crack propagation critical energy release rate G_{Ic}^{prop}, the crack initiation critical energy release rate G_{Ic}^{ini}, and the process zone length l_p.

The R-curve effect (i.e the increase of critical energy release rate with the crack length) is reproduced at constitutive level with the bilinear damage law indicated in Figure 16b. The law implemented is formed superimposing two linear damage laws, each of them representing a part of the tensile fracture process. A brittle linear damage law $d_{1+}^{l_1}(r_{1+})$ describes the crack initiation process, namely the breakage of the fibres in the warp tows. The fibre pullout and bridging mechanisms that cause the R-curve effect are reproduced with a tougher damage law $d_{1+}^{l_2}(r_{1+})$.

The superposition of the linear damage laws is defined by two parameters n_1 and m_1:

(i) The parameter n_1 is the ratio between the strength of the brittle linear law $X_T^{l_1}$ and the strength of the combined bilinear law X_T.

(ii) The parameter m_1 is the ratio between the fracture toughness of the brittle linear law $G_{1+}^{l_1}$ and the fracture toughness of the combined bilinear law G_{1+}.

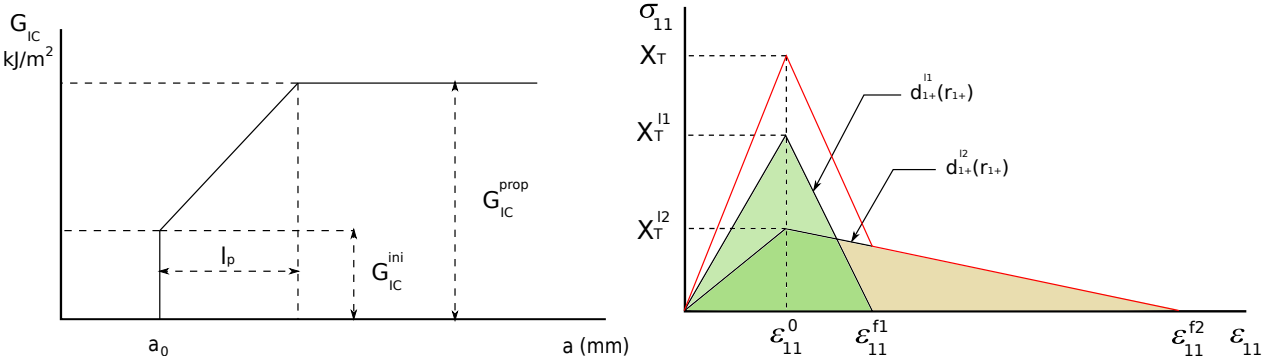

(a) Linear idealization of the resistance curve

(b) Bilinear damage law

Figure 16: Definition of the warp tension bilinear damage law linked to the linear idealized R-curve.

The superposition of the linear laws has to be defined such that, regardless of how they are combined, the resulting bilinear damage law is characterized by the same strength X_T and fracture toughness G_{1+}. For this reason, the strength and the fracture toughness of the brittle and tougher damage laws have to be complementary:

$$X_T^{l_1} = n_1 \; X_T \; ; \qquad X_T^{l_2} = (1 - n_1) \; X_T \tag{13}$$

$$G_{1+}^{l_1} = m_1 \; G_{1+} \; ; \qquad G_{1+}^{l_2} = (1 - m_1) \; G_{1+} \tag{14}$$

Furthermore, the regularization of the energy with the element size should be included in the formulation of each individual law. The objectivity of the numerical model has been ensured using Bazant's Crack Band Model [5]. Regardless of the element size, the areas shaded in Figure 16b are the objective fracture

toughnesses $G_{1+}^{l_1}$ and $G_{1+}^{l_2}$ per characteristic element length L_c. This is achieved defining the strains at which the entire energy is dissipated— and the crack propagates— as a function of the regularized fracture toughnesses, as follows:

$$\epsilon_{11}^{f_1} = \frac{2G_{1+}^{l_1}}{X_T^{l_1} L_c} \qquad \epsilon_{11}^{f_2} = \frac{2G_{1+}^{l_2}}{X_T^{l_2} L_c} \tag{15}$$

The formulation of the linear damage laws and their superimposition are presented respectively in the equations 16 and 17.

$$d_{1+}^{l_1} = \frac{\epsilon_{11}^{f_1}(r_{1+}\epsilon_{11}^0 - \epsilon_{11}^0)}{(r_{1+}\epsilon_{11}^0(\epsilon_{11}^{f_1} - \epsilon_{11}^0))} \qquad d_{1+}^{l_2} = \frac{\epsilon_{11}^{f_2}(r_{1+}\epsilon_{11}^0 - \epsilon_{11}^0)}{(r_{1+}\epsilon_{11}^0(\epsilon_{11}^{f_2} - \epsilon_{11}^0))} \tag{16}$$

$$d_{1+} = d_{1+}^{l_1} + d_{1+}^{l_2}(1 - n_1) \tag{17}$$

The shape of the bilinear damage law formulated in the equations presented above is determined by three input parameters: the fracture toughness of the law G_{1+}, and the ratios m_1 and n_1. These are defined based on the idealized R-curve (see Figure 16a), which can be measured with Compact Tension (CT) tests.

(i) The fracture toughness of the combined bilinear damage law G_{1+} corresponds to the crack propagation critical energy release rate G_{Ic}^{prop} of the R-curve.

$$G_{1+} = G_{Ic}^{prop} \tag{18}$$

(ii) The brittle linear law represents the crack initiation part of the fracture process. Therefore, its fracture toughness $G_{1+}^{l_1}$ must be set to match the crack initiation value G_{Ic}^{ini}, to which end the constant m_1 takes the form:

$$m_1 = \frac{G_{Ic}^{ini}}{G_{Ic}^{prop}} \tag{19}$$

(iii) The constant n_1 is the ratio between the strength of the brittle linear law $X_T^{l_1}$ and the strength of the combined bilinear law X_T. This parameter can be obtained based on the shape of the R-curve using the equation 20, derived by Davila [16]. In the expression of n_1, the constant γ is the process zone length factor, which takes different values depending on the process zone length model that is selected. The constants E and σ_c are the Young's modulus and the strength in longitudinal tension of the laminate used for measuring the R-curve with the compact tension test.

$$n_1 = 1 - \frac{2}{3}\gamma\frac{1 - m_1}{l_p}\frac{EG_{Ic}^{prop}}{\sigma_c^2} \tag{20}$$

It is important to note that, according to the failure criterion adopted, an effective in-plane shear stress $\hat{\tau_{12}}$ might promote tensile failure before reaching the strength allowable X_T (see equation 4). This situation corresponds to mixed-mode failure. The effective stress $\hat{\sigma_{11}}$ at which failure in a mixed-mode situation takes place is denoted as X_T^{MMF}. Logically, the critical energy release rate required to break the fibres is also lower than the one corresponding to the pure tensile mode. It is equally coherent to postulate that the toughening effects are also reduced by the damage in the matrix. The reason is that debondings and matrix splits caused by the shear mode diminish the fibre-matrix interface area, making easier the pull-out of the fibres. In order to take this into account, in a mixed-mode failure situation, the tensile fracture toughness G_{1+} is reduced based on the degree of mode mixity:

$$G_{1+}^{MMF} = G_{1+}\left(\frac{X_T^{MMF}}{X_T}\right)^2 \tag{21}$$

Figure 17 shows the tensile constitutive behavior affected by the interaction of an in-plane shear stress. The shaded area corresponds to the mixed-mode warp tensile fracture toughness per unit characteristic element length.

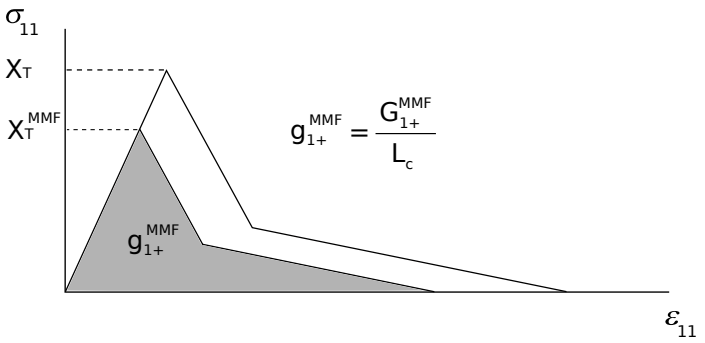

Figure 17: Schematic tensile constitutive behavior when a stress $\hat{\tau_{12}}$ is present.

3.3.2.2 Warp compression damage law

The definition of a damage law for compression $d_{1-}(r_{1-})$ capable of representing the softening behavior associated to this type of failure mode is out of the scope of this work. In this regard, the definition of a suitable damage law for describing the propagation of compression damage in macroscale CDM models for woven fabrics has not yet been developed. Pending further investigation in this particular aspect of the CDM model, an exponential damage law has been included for the compression failure modes in the warp and weft directions [7].

3.3.3 In-plane shear damage law

An exponential damage law has been chosen to describe the softening behavior in shear. The development of damage in shear is defined by the damage variable $d_6(r_6)$, which controls the degradation of the secant shear modulus remaining at failure initiation $G_{12}^*(\gamma_{12}^0)$ (see equation 10). The damage variable $d_6(r_6)$ depends on the failure function ϕ_6.

In Section 3.2, it was specified that the failure function ϕ_6 is computed according to the Maximum Stress criterion. This formulation is however used only for determining the damage onset. After the initiation of shear damage, in order to enforce that the evolution of the damage variable $d_6(r_6)$ causes the exponential softening of the modulus $G_{12}^*(\gamma_{12}^0)$, it is necessary to redefine the function ϕ_6 according to the following equation:

$$\phi_6 = \begin{cases} \dfrac{|\hat{\tau_{12}}|}{S_L}, & \text{if } d_6 = 0 \\ \dfrac{\mid G_{12}^*(\gamma_{12}^0)\ (\gamma_{12} - \gamma_{12p}^0)\mid}{S_L}, & \text{otherwise} \end{cases} \tag{22}$$

In order to simplify the model, the damage associated to in-plane shear has been considered to be orientationally invariant. That means that the generation of damage in the in-plane shear mode does not

[7] For a comprehensive description of the formulation of the exponential damage law, the reader is referred to the work of Maimi et al. [37].

distinguish between positive and negative shear. A threshold variable r_6 is defined based on the failure function ϕ_6 to ensure the non-reversibility of damage: [8]

$$r_6 = max\left(1, \phi_6, r_6^{t-1}\right) \tag{23}$$

The damage law $d_6(r_6)$ that has been adopted is the exponential function proposed by Maimi [37], and depicted in the equation 24.

$$d_6 = 1 - \frac{1}{r_6} e^{(A_6(1-r_6))} \qquad with \qquad A_6 = \frac{2L_c S_L^2}{2\ G_{12}^*(\gamma_{12}^0)\ G_6 - L_c S_L^2} \tag{24}$$

wherein G_6 is the in-plane shear fracture toughness, S_L the in-plane shear strength, L_c the characteristic element length, and $G_{12}^*(\gamma_{12}^0)$ the secant shear modulus at failure initiation. The constant A_6 is a closed form solution ensuring the regularization of the fracture energy with the element size. Figure 18a displays the in-plane shear constitutive behavior before and after failure initiation. The shaded area corresponds to the shear fracture toughness per unit element characteristic length.

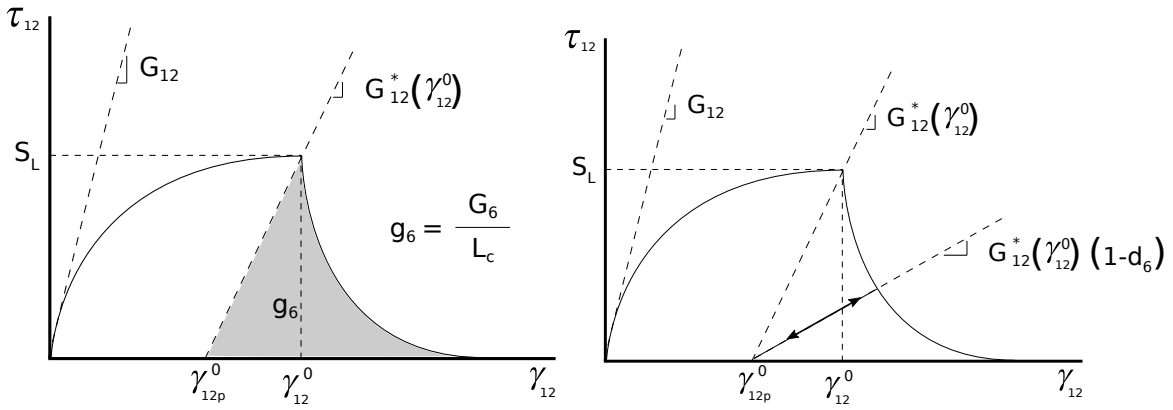

(a) Exponential damage law d_6 (b) Non-reversibility of damage

Figure 18: In-plane shear constitutive behavior after failure initiation

It should be noted that, if a situation were to occur in which the strain γ_{12} decreases after failure initiation, the non-reversibility condition established in equation 23 would result in the straight unloading path defined by the modulus $G_{12}^*(\gamma_{12}^0)(1-d_6)$, wherein d_6 is constant and equal to its value at the beginning of unloading. This situation is signaled in Figure 18b.

3.4 Conclusions

In this section, the continuum damage mechanics based model proposed for woven fabric composites has been described. The model has been coded as ABAQUS/Explicit VUMAT user-written subroutine. In order to ensure the objectivity of the numerical model, the fracture energy has been regularized using Bažant's Crack Band Model.

The non-linear shear behavior has been reproduced with a Ramberg-Osgood equation. Permanent deformation, and the degradation of the secant shear modulus have been coupled to the formulation of the unidimensional plasticity law. In tension, a bilinear damage law has been proposed to account for the toughening mechanisms associated to tensile failure. The bilinear damage law is formulated such that its input can be determined from the shape of a resistance curve measured with compact tension specimens. In addition, the interaction of shear stresses in the promotion of tensile failure has been taken into account at two levels: initiation and propagation. Failure initiation in tension is identified using Hashin's quadratic

[8] This expression complies with Kuhn-Tucker and consistency conditions reviewed in reference [37].

failure criterion. The effect of matrix cracks caused by shear loading in the propagation of tensile damage has been included by scaling the bilinear damage law according to the degree of mode mixity.

The following section details the methodology proposed for obtaining the input of the constitutive model corresponding to the tensile and in-plane shear modes. Specifically, the next section addresses the calibration of the shape of the bilinear damage law and the Ramberg-Osgood equation, the estimate of the interaction parameter included in Hashin's failure criterion, and the measurement of the secant shear modulus degradation.

4 Input of the constitutive model

The validation of the model has been performed comparing the strength prediction of unnotched and open hole coupons against experimental data from the NCAMP material data base [45]. The material system chosen for this purpose is a carbon/epoxy preimpregnated Hexcel AS4-8552-AGP193 plain weave fabric [24]. The material properties provided by the supplier and the ones made available by NCAMP are not enough to define the constitutive model proposed. This section presents the experimental work and simulations carried out to complement this information. In section 4.1, the determination of the properties defining the constitutive model in tension in the warp and weft directions is addressed. Section 4.2 explains the acquisition of the material data corresponding to the in-plane shear constitutive model. [9]

4.1 Input of the tensile constitutive model

The characterization of the constitutive model in tension in the warp and weft directions described in Section 3 requires the definition of the following properties:

(i) Elastic properties: E_1, E_2 and ν_{12}

(ii) Strength allowables: X_T and Y_T

(iii) Bilinear damage law input parameters: G_{1+}, n_1, m_1, G_{2+}, n_2 and m_2

(iv) Shear interaction parameters of the tensile failure criteria: α_1 and α_2

The aforementioned elastic properties and strength allowables of the lamina are readily available at the NCAMP material data base [45]. These values can be consulted in Tables 2 and 3.

E_1 (MPa)	E_2 (MPa)	ν_{12}
62087	62673	0.046

Table 2: Elastic properties

X_T (MPa)	Y_T (MPa)
751	742

Table 3: Tensile strength allowables

For a plain weave fabric, the properties in the warp and weft directions are indistinct [10]. Therefore, the bilinear damage law input parameters associated to the warp direction (G_{1+}, n_1 and m_1) and the ones corresponding to the weft direction (G_{2+}, n_2 and m_2) are the same. Similarly, the same interaction parameter can be considered for the tensile failure criterion associated to the warp direction (α_1) and the one corresponding to the weft direction (α_2).

The bilinear damage law input parameters can be obtained from the shape of the linear idealized R-curve.

4.1.1 Measurement of the resistance curve

In order to determine the R-curve, experimental data from Compact Tencion (CT) tests of $[90]_{16}$ laminates have been used. The load-displacement curves and digital image correlation (DIC) raw data issuing from testing five CT specimens, whose geometry corresponds to the one proposed by Pinho [48] (see Figure 8), were provided by IMDEA Materials. The load-displacement curves have been included in Figure 19.

It can be noticed that the loss of stiffness taking place during the fracture process is marked by large load drops. These drops, which are accompanied by abrupt crack openings, underline the unstable nature of the crack propagation. Only during the stages in which simultaneously the load increases and the crack

[9] The elastic constants, strength allowables and fracture toughness associated to the other failure modes are not relevant in this study. For the sake of completeness the values adopted have been included in Table 10.

[10] The small differences in the values presented in Tables 2 and 3 are due to the material scatter.

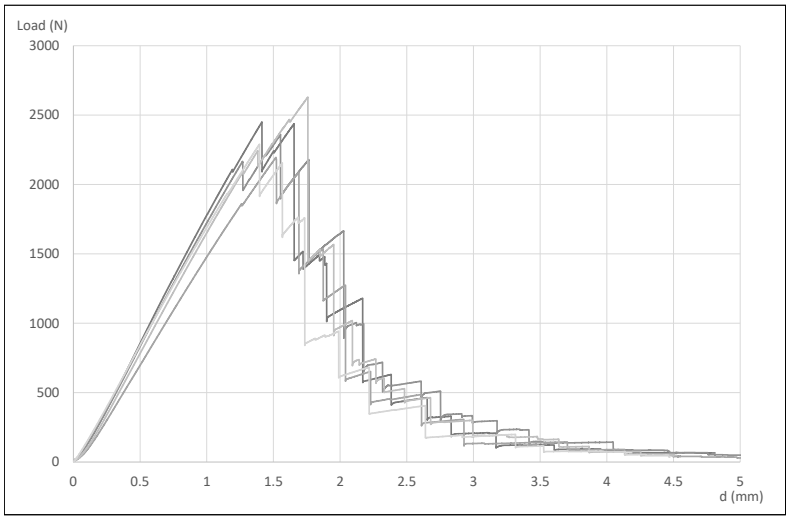

Figure 19: Experimental CT load-displacement curves

opens, a steady crack growth can be assumed [19]. For each of these stages, the critical energy release rate has been measured at the peak before the load drop.

The Compliance Calibration (CC) Method is the approach selected for obtaining the critical energy release rate. Particularly, the data reduction methodology developed by Gutkin et al. [21] has been adopted. In their work, the compliance of the system C is considered to be a function of the instantaneous crack length a, which is optically measured. This function, is calibrated using as physical reference the quotient between the displacement and the load ($C = d/P$) measured in the tests. The critical energy release rate is then computed using the relation given by the equation 25, wherein P_c is the critical load causing the crack opening, t is the thickness of the specimen, and $dC(a)/da$ is the change of the specimen compliance with the crack length.

$$G_{Ic} = \frac{P_c}{2\ t}\ \frac{dC(a)}{da} \tag{25}$$

For determining the critical energy release rate, it is required to define a differentiable function $C(a)$. Gutkin et al. [21] propose the function taking the following form:

$$C(a) = (\zeta a + \beta)^{\chi} \qquad \text{where} \qquad \zeta,\ \beta,\ \text{and}\ \chi\ \text{are fitting parameters} \tag{26}$$

Adding a constant c to the expression above seems to enable a better fit of the experimental values corresponding to the crack initiation. Accordingly, the expression below has been used:

$$C(a) = c + (\zeta a + \beta)^{\chi} \qquad \text{where} \qquad c,\ \zeta,\ \beta,\ \text{and}\ \chi\ \text{are fitting parameters} \tag{27}$$

The compliance of the specimens is shown in Figure 20, wherein each symbol type corresponds to the data obtained with a single specimen. It has been noticed that the measurement of the critical energy release rate is very sensitive to the fit of $C(a)$ at high values of crack length a. Therefore, instead of fitting the data cloud with the constants c, ζ, β and χ providing the closest regression, two calibration bounds have been defined.

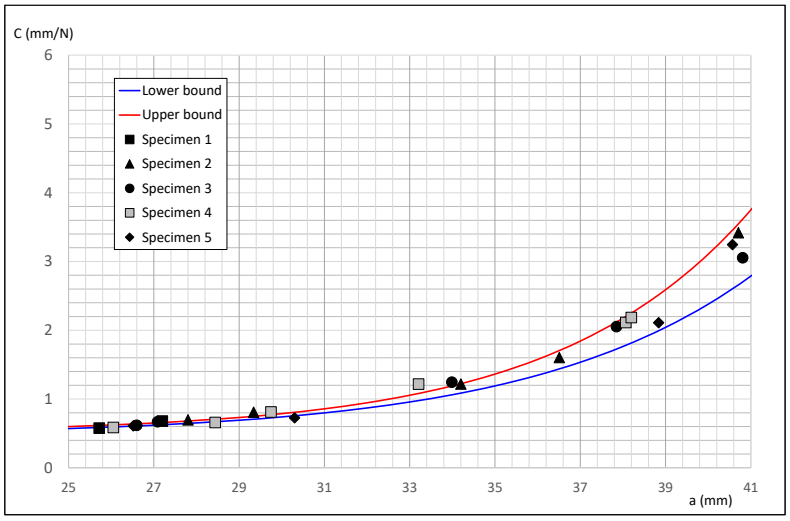

Figure 20: Compliance C vs. instantaneous crack length a. Lower bound fitting constants: c=0.47 ζ=0.001445 β=0.9475 and χ=131. Upper bound fitting constants: c=0.51 ζ=0.00154 β=0.945 and χ=145.

Equation 25 yields the R-curves presented in Figures 21a and 21b for each of the calibration bounds depicted in Figure 20. Again, each symbol type corresponds to the data obtained with a single specimen. A neat R-curve effect is considerable for both estimates. Clearly, the error provided by the CC method increases with the crack length. This is probably due to the unstable nature of the crack propagation and the development of other damage mechanisms besides the ones associated to intralaminar tension.

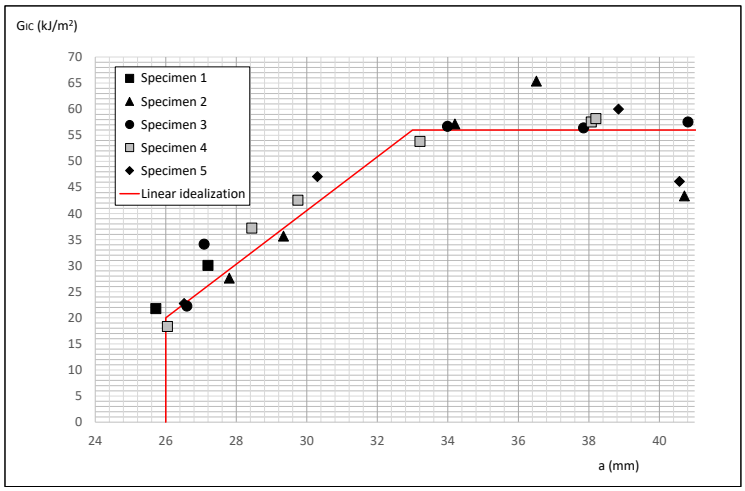

(a) Resistance curve with the upper bound fit of the compliance

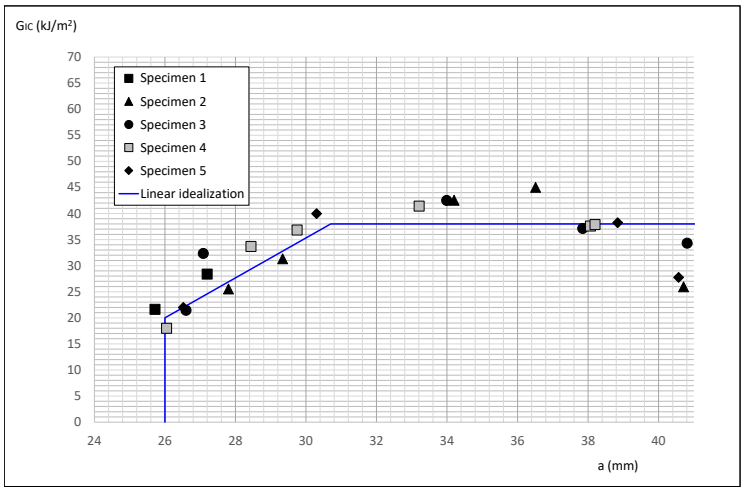

(b) Resistance curve with the lower bound fit of the compliance

Figure 21: Resistance curves obtained with the CC method.

In the Figures 21a and 21b alongside the experimental results, a linear idealization has been proposed. As was mentioned in Section 3.3.2, the constants defining the linear idealized R-curve are: the crack propagation critical energy release rate G_{Ic}^{prop}, the crack initiation critical energy release rate G_{Ic}^{ini}, and the process zone length l_p (see Figure 16a). The values of the constants yielding the idealization presented in Figures 21a and 21b can be found in the Table 4. It can be noticed that, although the same initiation value has been identified in the R-curves obtained with the different compliance calibrations, the difference in the propagation values is significant.

	G_{Ic}^{ini} (kJ/m^2)	G_{Ic}^{prop} (kJ/m^2)	l_p (mm)
Upper bound	20	56	7.0
Lower bound	20	38	4.7

Table 4: Linear idealized R-curve constants obtained with the lower and upper bound fits of the compliance

In order to select a suitable crack propagation critical ERR within the limits provided by the CC Method— $G_{Ic}^{prop} \in [38; 56]$ kJ/m^2, a second data reduction technique has been applied: the Area Method [19, 31]. In this method, the fracture toughness is computed as the quotient between the energy consumed during the crack growth E_c, and the area swept by the crack front A_c (see equation 28). The energy consumed during the crack growth E_c is directly obtained from the load-displacement curve. A graphical representation of the measurement of this property has been included in Figure 22. The area swept by the crack front A_c is computed from the thickness of the specimen t, and the increment of crack length $\Delta a = a - a_0$ [11].

$$G_{Ic} = \frac{E_c}{A_c} \qquad \text{with} \qquad A_c = \Delta a \; t \tag{28}$$

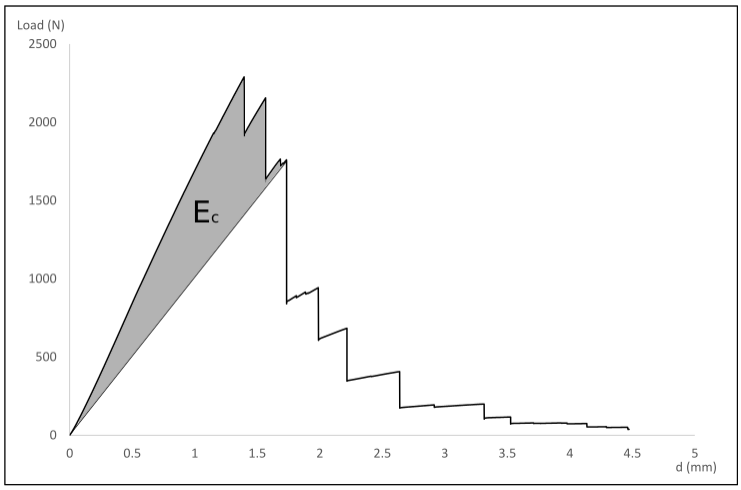

Figure 22: Example of measurement of the energy consumed during crack growth

The evolution of the critical ERR with the crack length obtained with the Area Method is shown in Figure 23. The increasing values of critical ERR indicate a toughening effect. Nonetheless, it is not possible to clearly identify an initiation value. It would thus appear that this data reduction technique only provides consistent values once the fracture process is fully developed. In this regard, the critical ERR stabilizes— for crack lengths above 33 mm— at a propagation level corresponding to $G_{Ic}^{prop} = 40$ kJ/m^2.

[11] The constant a_0 is the initial crack length. For the geometry of the CT specimens provided, corresponding to the one proposed by Pinho [48] (see Figure 8), it is equal to 26 mm.

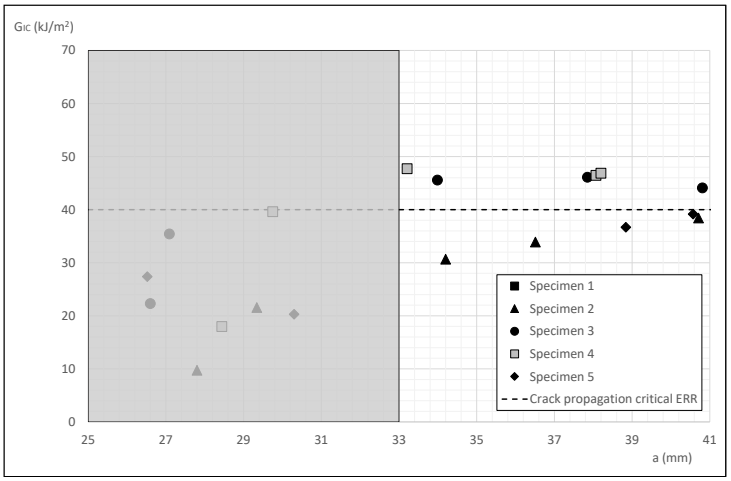

Figure 23: Crack propagation critical ERR measured with the Area Method

In view of the results obtained with the Compliance Calibration Method and the Area Method, the crack initiation critical ERR, the crack propagation critical ERR, and length of the process zone that will be used for defining the bilinear damage law are:

G_{Ic}^{ini} (kJ/m^2)	G_{Ic}^{prop} (kJ/m^2)	l_p (mm)
20	40	5.0

Table 5: Constants of the linear idealized R-curve used for defining the bilinear damage law

The length of the process zone l_p has been obtained interpolating linearly between the crack propagation critical ERR's found with the CC Method for each calibration bound with the value $G_{Ic}^{prop} = 40\ kJ/m^2$ obtained from the Area Method.

4.1.2 Calibration of the bilinear damage law

In the constitutive model, the shape of the bilinear damage law is controlled by the parameters G_{1+}, n_1 and m_1. These parameters were defined in Section 3.3.2 as a function of the constants describing the linear idealization of the R-curve: G_{Ic}^{ini}, G_{Ic}^{prop} and l_p. In the interest of clarity, the equations 18 – 20 are re-stated below:

$$G_{1+} = G_{Ic}^{prop}\ ; \qquad m_1 = \frac{G_{Ic}^{ini}}{G_{Ic}^{prop}}\ ; \qquad n_1 = 1 - \frac{2}{3}\gamma\frac{1-m_1}{l_p}\frac{EG_{Ic}^{prop}}{\sigma_c^2} \tag{29}$$

In order to relate the R-curve to the bilinear damage law, the process zone length factor γ has to be specified, along with the Young's modulus E and the strength σ_c of the CT laminate in tension. The process zone length factor depends on the process zone length model that is chosen. Davila [16] suggests to use for UD carbon/epoxy composites the model proposed by Hillerborg et al. [25], wherein γ is equal to 1.0. In the absence of a process zone length model specific for woven fabrics, same value has been selected. Since the CT laminate has a $[90]_{16}$ stacking sequence, the constants E and σ_c correspond to the ply properties E_2 and Y_T respectively. Although strictly the R-curve measured corresponds to the weft direction, it is recalled that in the material system chosen the properties in the warp and weft directions are analogous.

The bilinear damage law parameters obtained with the R-curve linear idealization constants depicted in Table 5 using the equations 18 – 20, are indicated in Table 6.

G_{1+} (kJ/m^2)	m_1	n_1
40	0.50	0.70

Table 6: Bilinear damage law input parameters obtained from the R-curve.

In order to verify that the bilinear damage law defined by these input parameters is able to faithfully represent the energy dissipation during the fracture process, a finite element model for Abaqus/Explicit of the CT test with 3D elements has been performed (see Figure 24). The idea is to compare the load-displacement curve obtained from the simulation against the experimental data. The constitutive model incorporating the tensile damage law has been applied exclusively in the band of elements located in the ligament of the specimen in front of the precrack, indicated in Figure 25. In the other regions, an elastic orthotropic behavior has been assumed. The element size in the region where the constitutive damage model is applied is 0.2 mm. To make possible the comparison between the experimental results and the FE simulation, it is necessary to obtain a similar compliance. How the load introduction is modeled has a great effect on this. Using Multi-Point Constraints overlooks the slippage of the pins and leads to an overly stiff response. For that reason, it has been chosen to model the pins and their contact with the laminate. The pins have been modeled as rigid analyical surfaces, and the contact as a surface to surface contact, allowing for slippage with tangential friction (with a friction coefficient equal to $\eta = 0.15$).

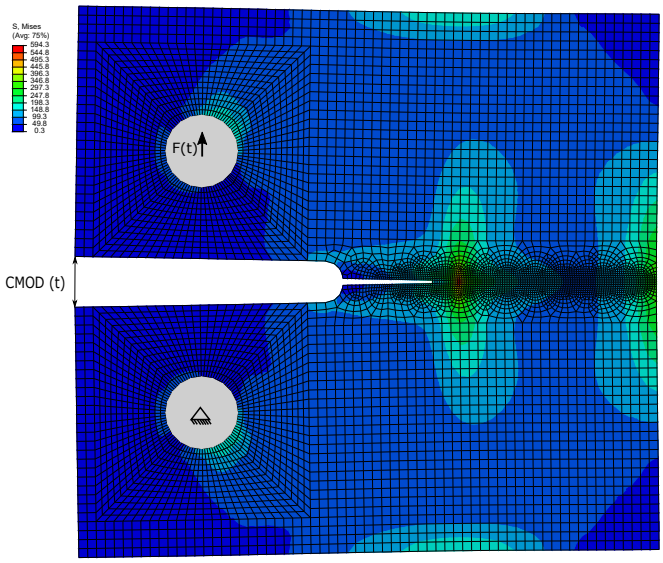

Figure 24: Compact Tension FE model

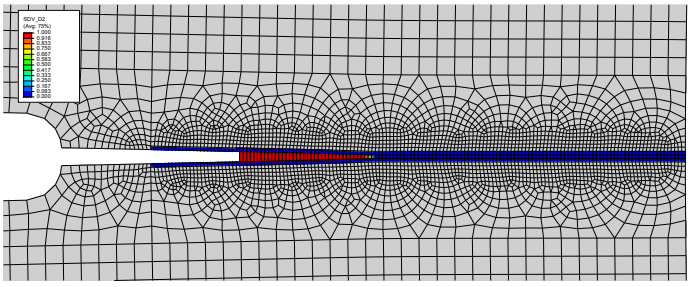

Figure 25: Detail of the band of elements where the CDM model is applied. Plotted: damage variable d_2

Another important aspect to note is that, due to the compliance of the load cell, the displacement given by the test machine does not correspond with the displacement of the pin. As a result it is not possible to compare the reaction force versus displacement of the pin in the FE model against the experimental data presented in Figure 19. To bypass the compliance of the machine, instead of using the displacement of the pin, it has been chosen to work with the Crack Mouth Opening Displacement (CMOD) indicated in Figure 24. This magnitude has been tracked optically in the experimental tests employing DIC.

Figure 26 shows the Force-CMOD response predicted by the FE model against the experimental results. It can be observed that the stiffness is well predicted by the FE model and that a good correlation of the softening associated to the fracture process has been found. The maximum load predicted is however equal to 2530 N, which is 15 % higher than the average load of the experimental tests at the same CMOD. This mismatch is attributed to the homogenization of the fabric properties:

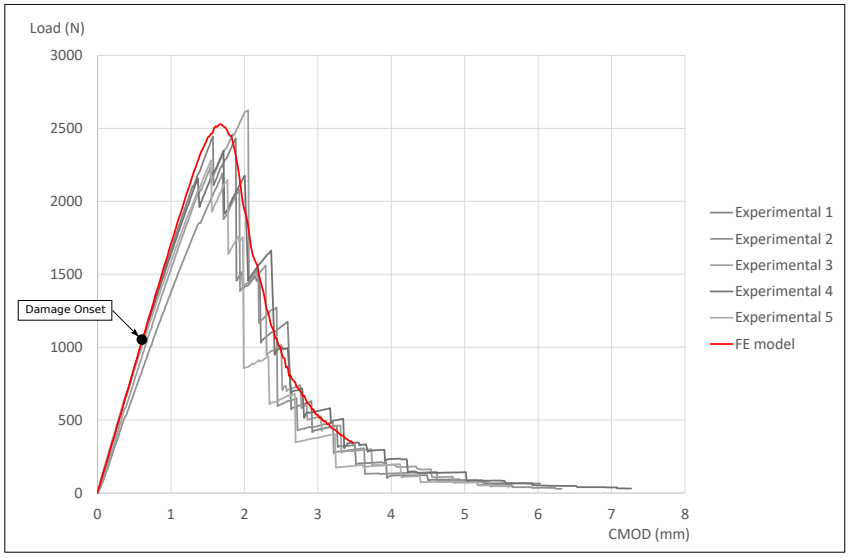

Figure 26: Force-CMOD curve predicted with the compact tension FE model using the bilinear damage law defined from the idealized resistance curve.

The characteristic element size in the band of elements where the constitutive model is applied (i.e in front of the pre-crack) is 0.2 mm, which is approximately ten times lower than the width of the fabric tows. In the range of 0.2 mm in front of the crack, the tensile stress that is actually required to cause failure initiation is the tensile strength in the tow containing the tip of the crack and oriented perpendicular to the crack propagation direction. This strength is higher than the homogenized tensile strength[12]. The onset of damage locally takes place at high stress level, and it is followed by a steep stiffness drop characteristic of the brittle failure of the fibres. Instead, in the homogenized CDM model, the tensile strength is lower. Because of this, the fracture energy after failure initiation— which is determined by the R-curve— is dissipated very gradually. The more gradual the damage law is, the more load the specimen can bear after the onset of damage— point indicated in Figure 26— before collapsing. This results in the overprediction of the maximum load mentioned above.

In short, since the homogenized tensile strength does not correspond with the local strength in the vicinity of the crack tip, the critical energy release rate that the elements in the model should display after failure initiation to reproduce the crack opening does not correspond to the resistance curve measured with CT tests. This is a limitation intrinsic of modeling 2D woven composites with the homogenized CDM approach.

In order to circumvent this problem, an alternative procedure for defining the shape of the bilinear damage law is proposed:

[12]Essentially, because the volumetric fraction of fibres aligned in the tensile direction is higher.

The alternative consists in calibrating the bilinear damage law parameters G_{1+}, n_1, and m_1 by matching the prediction of the CT Force-CMOD curve obtained from FE analysis to the experimental results.

Basically, the engineering solution proposed to the problem associated to the homogenization is to use the compact tension FE model for calibration, instead that for verifying that the shape of the bilinear damage law obtained from the linear idealized R-curve is able to represent the fracture process. From a practical point of view, it is important to emphasize that this methodology does not require any additional experimental test, as the CT test data was anyhow needed for defining the tensile damage law. Also, it does not conflict with the validation of the constitutive model, since this one is carried out using complete separate experimental results.

The bilinear damage law parameters G_{1+}, n_1, and m_1 that result in a perfect match of the experimental Force-CMOD curves are presented in Table 7. Figure 27 illustrates the fit of the experimental Force-CMOD curves achieved with these parameters.

G_{1+} (kJ/m^2)	m_1	n_1
34	0.375	0.750

Table 7: Bilinear damage law input parameters calibrated using the compact tension FE model.

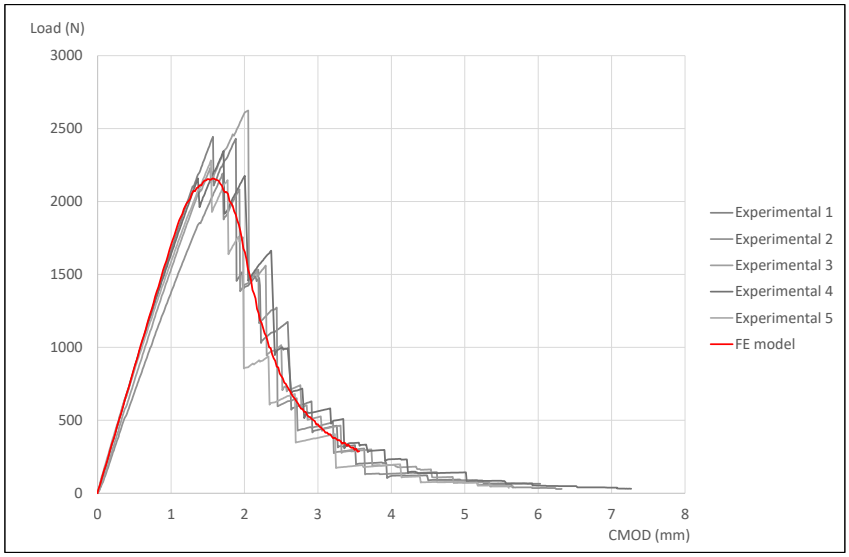

Figure 27: Force-CMOD curve predicted with the compact tension FE model using the bilinear damage law calibrated using the FE model.

Figure 28 includes a comparison of the bilinear damage law obtained from the idealized resistance curve measured with CT tests— Figure 28a— and the bilinear damage law calibrated using the compact tension FE model— Figure 28b. It can be noticed that the bilinear damage law obtained by calibration is characterized by being steeper than the one obtained from the resistance curve. This goes in the line with the explanation provided above regarding the homogenization of the fabric properties.

The bilinear damage law that will be used for the validation of the constitutive model in Section 5 is the one obtained by calibration using the compact tension FE model.

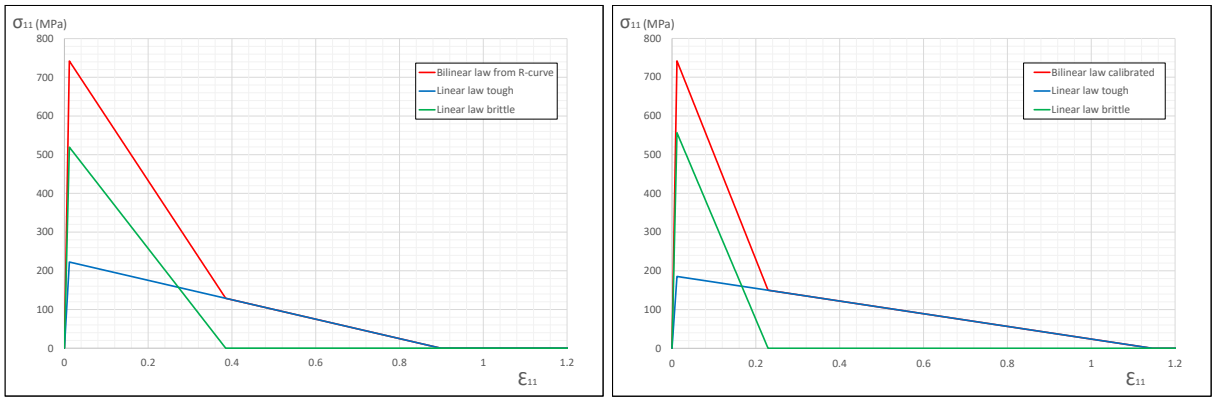

(a) Bilinear damage law obtained from the idealized resistance curve measured with compact tension tests.

(b) Bilinear damage law calibrated using the compact tension FE model

Figure 28: Comparison of the tensile damage laws associated to the input parameters of Tables 6 and 7.

4.1.3 Estimate of the interaction parameter of the tensile failure criterion

The parameter α_1 in equation 4 controls the shape of the failure envelope $\hat{\sigma_{11}}$–$\hat{\tau_{12}}$. As such, it defines the point in the failure envelopes at which failure initiation is triggered simultaneously in tension and shear. This point can be reverse engineered based on the estimation of the ply orientation at which the failure mode identified in an off-axis tension test switches from tensile failure to shear failure.

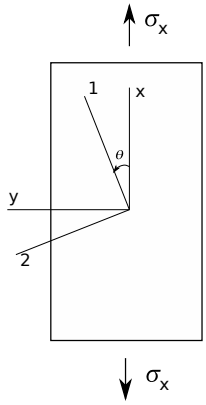

Figure 29: Schematic representation of a $[\theta]_{ns}$ off-axis tension test

In an off-axis $[\theta]_{ns}$ tension test, the ratio between the effective stress components $\hat{\sigma_{11}}$ and $\hat{\tau_{12}}$ in local coordinates can be obtained from the ply orientation θ.

$$\frac{\hat{\sigma_{11}}}{\hat{\tau_{12}}} = \frac{1}{-tan(\theta)} \tag{30}$$

The failure mode will change from tension to shear for a critical angle θ_c. At this angle, the following conditions must be satisfied:

$$\phi_{1+} = \left(\frac{\hat{\sigma_{11}}}{X_t}\right)^2 + \alpha_1 \left(\frac{\hat{\tau_{12}}}{S_L}\right)^2 = 1 \tag{31}$$

$$\phi_6 = \frac{|\hat{\tau_{12}}|}{S_L} = 1 \tag{32}$$

Combining equations 30, 31 and 32 it is possible to formulate the parameter α_1 as a function of the angle θ_c and the strength allowables of the ply X_T and S_L.

$$\alpha_1 = 1 - \left(\frac{S_L}{X_T \ tan(\theta_c)} \right)^2 \tag{33}$$

The estimation of the critical angle θ_c has been based on the examination of experimental axial stress-strain curves from off-axis tests available in the literature. Naik et al. [43] studied the tensile response of plain weave carbon/epoxy laminates with different ply orientations 0°, 15°, 30° and 45°. It was found that the local shear stress at failure of the coupon with off-axis angle $\theta = 15°$ matched the one with off-axis angle $\theta = 45°$. In addition, the axial stress-strain response obtained for $\theta = 15°$ displayed, to some degree, nonlinearity. Accordingly, it has been considered that for $\theta = 15°$ the failure mode is shear. In view of this consideration and pending further experimental characterization with lower orientations, it has been decided to select a slightly lower critical off-axis angle: $\theta_c = 13°$ leading to the input parameter $\alpha_1 = 0.7$.

4.2 Input of the in-plane shear constitutive model

The in-plane shear constitutive behavior described in Section 3 requires the definition of the following input properties:

(i) Ramberg-Osgood law constants: G_{12}, ρ, and τ_{12}^a

(ii) In-plane shear strength: S_L

(iii) In-plane shear fracture toughness: G_6

(iv) Evolution of the secant shear modulus: $G_{12}^*(\gamma_{12})$

4.2.1 In-plane shear test

A tensile test of a $[\pm 45]_{3s}$ laminate has been conducted according to the standard ASTM D3518 [4] with an INSTRON 3384 electromechanical machine. Digital image correlation was used for measuring the longitudinal and transversal average strains in an area of interest, ϵ_x and ϵ_y respectively. The shear strain was obtained using the relation $\gamma_{12} = \epsilon_x - \epsilon_y$. The shear stress was computed according to the equation 34, wherein P is the load measured by the load cell, and A is the cross-sectional area of the specimen.

$$\tau_{12} = \frac{P}{2A} \tag{34}$$

Figure 30a shows the fracture area of the failed specimen. Rotation of the tows, fibre pull-out and fibre breakage can be observed. The shear stress-strain curve resulting from this test is included in Figure 30b. For relatively low shear strains, the behavior is non-linear due to the accumulation of damage and plasticity in the matrix. Then, the tangent stiffness gradually levels off, and the response becomes progressively dominated by the reorientation of the fibre bundles towards the loading direction (i.e the trellis effect). Eventually, at $\gamma_{12} = 21.8\%$, the specimen fails due to fibre breakage.

At the constitutive level, the response of the material in shear should transition from hardening to softening at a high shear strain. This transition and the subsequent softening is overshadowed by the stiffening caused by the trellis effect. Therefore, it is not possible to obtain a physical reference exclusively of the shear constitutive behavior for high stages of deformation with an in-plane shear test. This implies that the curve presented in Figure 30b provides no information about at which stress shear failure initiation takes place. Nevertheless, as was pointed out by Iannucci [28], laminates complying with the 10 % design rule fail way before high shear strains are reached due to the tensile failure of the laminas with orientations 0° and 90°. Therefore, the definition of the shear constitutive behavior for high stages of deformation is irrelevant to achieve the objective of this work. Additional experimental work for obtaining the in-plane shear strength

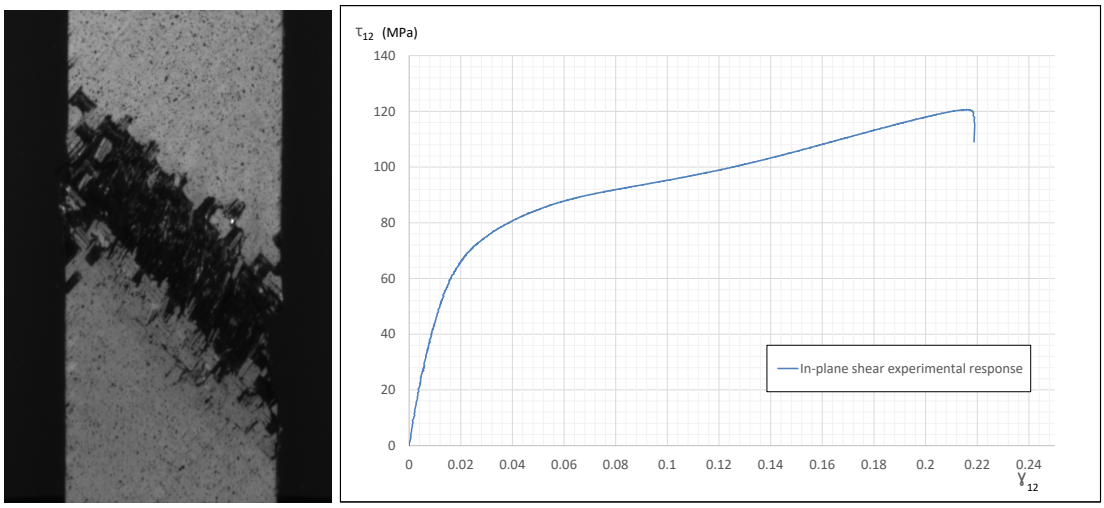

(a) Fracture of the specimen (b) Shear stress-strain curve

Figure 30: Results of the tensile test of a $[\pm 45]_{3s}$ unnotched coupon.

S_L and the fracture toughness G_6 is not needed because these material properties do not have any impact in the ultimate strength prediction of coupons with conventional stacking sequences [13].

With this in mind, it has been decided to arbitrarily assume that the strain $\gamma_{12} = 10\%$ corresponds to the strain at shear failure initiation. The Ramberg-Osgood law constants G_{12}, ρ, and τ_{12}^a have been chosen to fit the experimental shear constitutive relation up to this strain. The constants that have been selected for this purpose are indicated in Table 8. Figure 31 illustrates the fit obtained. The in-plane shear strength S_L is the stress level corresponding to the strain $\gamma_{12} = 10\%$. The values selected for the strength S_L and the fracture toughness G_6 can be consulted in Table 10.

G_{12} (MPa)	ρ	τ_{12}^a (MPa)
6232	1.286	101.7

Table 8: In-plane shear Ramberg-Osgood constants

[13] This was corroborated carrying out a sensitivity study. Differences smaller than 1 % in the ultimate strength prediction of the coupons used for the validation of the constitutive model were found for upper and a lower bound values of S_L and G_6.

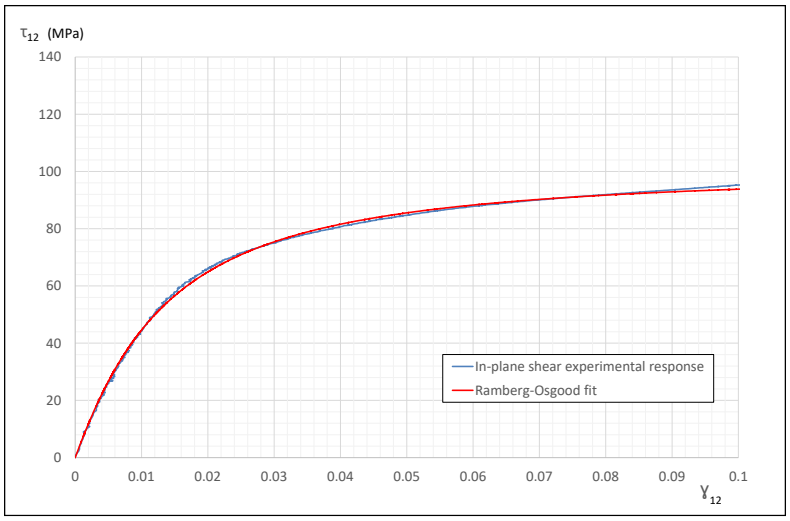

Figure 31: Fit of the in-plane shear response with Ramberg-Osgood equation.

4.2.2 Cyclic in-plane shear test

Four cyclic in-plane shear tests (ASTM D3518/D3518M-94 [4]) have been carried out in order to obtain the evolution of the secant modulus with the strain. Coupons with stacking sequences $[\pm 45°]_{3s}$ were subjected to tensile loading-unloading cycles of increasing amplitude at a constant velocity of 2 mm/min. Figure 32 depicts the cyclic stress-strain response obtained for one of the coupons tested. The complete set of cyclic shear stress vs. strain curves can be consulted in Annex B.

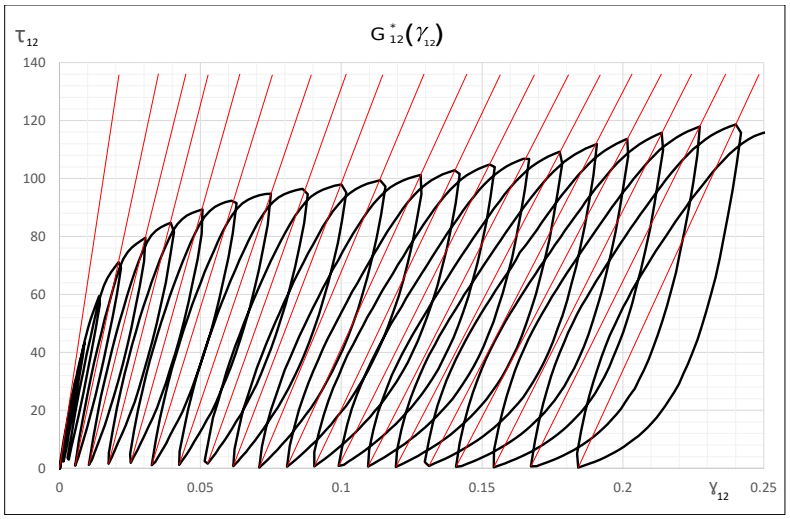

Figure 32: In-plane shear stress vs. strain relation obtained from the cyclic tensile test of a $[\pm 45°]_{3s}$ laminate.

The evolution of the modulus G_{12}^{*} with the shear strain γ_{12} caused by the accumulation of damage in the matrix is presented in Figure 33 for the four specimens tested. The data has been fitted with the double exponential law indicated in the equation 35. The use of this function was originally suggested by Tan [53]. The values of the fitting constants c_1, c_2, c_3, and c_4 in the aforementioned equation are specified in Table 9. For low shear strains, the fit has been extrapolated towards the pristine modulus G_{12} obtained from the

non-cyclic test.

$$G_{12}^{*}(\gamma_{12}) = c_1 e^{c_2|\gamma_{12}|} + c_3 e^{c_4|\gamma_{12}|} \tag{35}$$

c_1	c_2	c_3	c_4
3995	-24.89	2121	-0.7876

Table 9: Constants defining the secant shear modulus function.

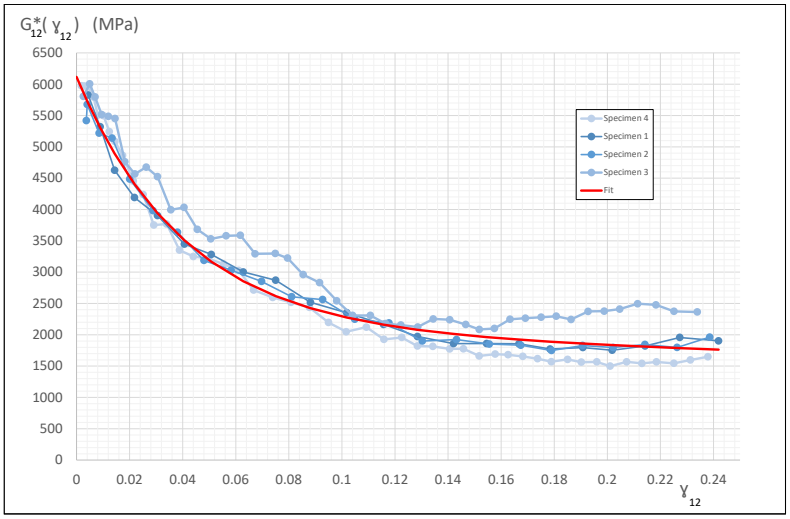

Figure 33: Evolution of the secant shear modulus and fit provided by the double exponential function.

It can be observed that the secant shear modulus is drastically reduced by the accumulation of damage in the matrix. Also, the stiffness degradation visibly decreases with the strain. The modulus seems to stabilize for values around $G_{12}^{*} = 2000MPa$, corresponding to 32 % the pristine modulus G_{12}. The experimental response obtained from the cyclic in-plane shear tests is also affected by the trellis effect. In this regard, fibre rotation might be mitigating the effect of the accumulation of damage in the matrix for high shear strains.

4.3 Conclusions

In this section is has been detailed the methodology proposed for obtaining the input of the constitutive model corresponding to the tensile and in-plane shear modes. The material system used as reference in this work is the carbon/epoxy AS4-8552-AGP193 plain weave fabric.

The shape of the bilinear damage law was calibrated using compact tension test results. These results were post-processed using two data reduction techniques: the compliance calibration method and the area method. Although the results displayed a certain level of scatter, a reasonable linear idealized resistance curve could be proposed. The shape of the linear idealized resistance curve was then linked to the parameters defining the bilinear damage law. A finite element model of the compact tension test was carried out to verify that the bilinear damage law defined by this method is able to faithfully represent the energy dissipation during the tensile fracture process. The FE model was not capable of predicting accurately the peak load of the test. The mismatch was attributed to the homogenization of the fabric properties, and revealed a potential limitation of modeling 2D woven composites with the homogenized CDM approach. In view of this, an engineering solution for determining the shape of the bilinear damage law was proposed. The procedure

consists in calibrating the law by matching the prediction of the CT Force-CMOD curve obtained from FE analysis to the experimental results.

For obtaining the input necessary to define the shear behavior in the constitutive model, off-axis tensile tests of $[\pm 45]_{3s}$ laminates were conducted. The constants defining the Ramberg-Osgood law were calibrated using a conventional off-axis tensile test, whereas the evolution of the secant shear modulus with the strain was obtained from a set of cyclic off-axis tensile tests. This methodology for defining the input of the shear constitutive response was found convenient, since only a limited amount of experimental tests of coupons in tension is required.

5 Verification and validation of the constitutive model

The constitutive model has been validated including it in a set of FE models of unnotched and open hole coupons, and comparing the ultimate strength predicted by the simulation of the coupons against an experimental benchmark.

As previously mentioned, the material system used for the validation is the carbon/epoxy plain weave fabric AS4-8552-AGP193. The input properties of the constitutive model associated to this material can be consulted in Table 10. In the interest of clarity, the properties that are relevant in this work have been highlighted.[14]

Elastic properties			
$E_1 = 62087(MPa)$	$E_2 = 62673(MPa)$	$E_3 = 10000(MPa)$	
$\nu_{12} = 0.046$	$\nu_{13} = 0.35$	$\nu_{23} = 0.35$	
$G_{12} = 6232(MPa)$	$G_{13} = 6232(MPa)$	$G_{23} = 6232(MPa)$	
Strength properties			
$X_T = 751(MPa)$	$X_C = 793(MPa)$	$Y_T = 742(MPa)$	$Y_C = 752(MPa)$
$Z_C = 600(MPa)$	$S_L = 93.8(MPa)$	$S_R = 93.8(MPa)$	
$\alpha_1 = 0.7$	$\alpha_2 = 0.7$		
In-plane shear constants			
$\rho = 1.286$	$\tau_{12}^a = 101.7(MPa)$		
$c_1 = 3995$	$c_2 = -24.89$	$c_3 = 2121$	$c_4 = -0.7876$
Fracture toughness properties			
$G_{1+} = 34(kJ/m^2)$	$G_{1-} = 20(kJ/m^2)$	$G_{2+} = 34(kJ/m^2)$	$G_{2-} = 20(kJ/m^2)$
$G_6 = 34.4(kJ/m^2)$	$G_{3-} = 12.5(kJ/m^2)$	$G_4 = 12.5(kJ/m^2)$	$G_5 = 12.5(kJ/m^2)$
$n_1 = 0.750$	$m_1 = 0.375$	$n_2 = 0.750$	$m_2 = 0.375$

Table 10: Input material properties of the constitutive model. Material system AS4-8552-AGP193.

5.1 Experimental Benchmark

The experimental benchmark has been obtained from the NCAMP material database [45]. It corresponds to the ultimate strength of six coupons under tensile loading. Three coupons are unnotched, and the other three are open hole coupons. For each type, every coupon has a different stacking sequence. The stacking sequences are:

(i) Quasi-isotropic laminate: $[45/0/\text{-}45/90]_{2s}$

(ii) Soft laminate: $[45/\text{-}45/0/45/\text{-}45/45/\text{-}45/90/45/\text{-}45]_s$

(iii) Hard laminate: [0/90/0/45/90/0/90/-45/90/0/90/45/0/90/0]

For each type of coupon and stacking sequence the results corresponding to 19-21 specimens are provided. Table 11 indicates the average, minimum and maximum ultimate strength of these tests for each coupon configuration. In order to simplify the notation, hereinafter the following nomenclature will be adopted:

UNT/OHT XYZ

wherein "UNT" indicates unnotched, "OHT" open hole; and "X", "Y" and "Z" corresponds to the first digit of the percentage of plies in the laminate having the orientation 0°, ±45° and 90° respectively. Examples of this notation can be found in Table 11.

[14]The rest of properties are either provided by the supplier or estimated based on the literature.

Nomenclature	Laminate	No. Specimens	Strength (MPa)		
			Average	Minimum	Maximum
UNT252	$[45/0/-45/90]_{2s}$	19	583.4	534.1	650.3
UNT181	$[45/-45/0/45/-45/45/-45/90/45/-45]_s$	20	378.6	355.2	413.7
UNT424	[0/90/0/45/90/0/90/-45/90/0/90/45/0/90/0]	21	685.6	643.7	736.6
OHT252	$[45/0/-45/90]_{2s}$	19	297.4	264.4	336.5
OHT181	$[45/-45/0/45/-45/45/-45/90/45/-45]_s$	19	302.6	279.4	320.8
OHT424	[0/90/0/45/90/0/90/-45/90/0/90/45/0/90/0]	19	349.4	312.1	386.5

Table 11: Experimental benchmark results used for validating the constitutive model [45].

According to the NCAMP technical report [45], the tests were conducted following the standard procedure ASTM D3518 [4] for the unnotched coupons, and ASTM D5766 [3] for the open hole coupons.

5.2 Finite element models of the unnotched and open hole coupons

A Python script provided by IMDEA Materials has been used to build the FE models of the coupons[15]. The finite element models are developed for Abaqus/Explicit.

In this type of simulation, there are numerous sources of non-linearity, among them a material constitutive behavior accounting for damage, large deformations and contact definitions. With diverse sources of non-linearity, implicit integration requires a large amount of iterations until reaching the equilibrium solution. At every iteration the stiffness and mass matrices are inverted, in practice resulting in excessive calculation times. In an explicit integration scheme, the central difference method is used over a time increment to compute the solution. As a result, explicit numerical integration requires instead a large number of less computationally expensive increments, which is —under these circumstances— generally more efficient [36].

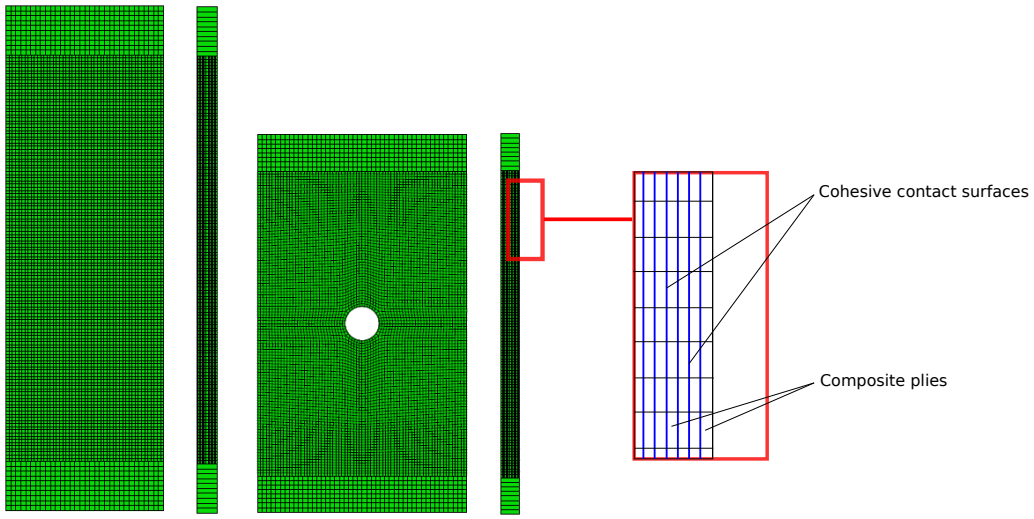

Figure 34: Schematic figure of the coupon FE models and the ply-by-ply discretization

The FE models use 3D elements to model the plies. In particular, each ply is modeled as a layer of C3D8R brick elements. Between each pair of plies, a cohesive contact surface is defined in order to model interlaminar damage. Section 5.2.1 describes with more detail how interlaminar damage is modeled. The ply-by-ply discretization is illustrated in Figure 34. For introducing the load, a velocity is imposed in one

[15]The authorship of the script is not claimed by the author of this document.

end of the coupon, whereas the other end is pinned. Rotation of the coupons along the longitudinal axis is restricted.

The element size must be chosen such that the intralaminar and the interlaminar damage mechanisms are well represented. On the other hand, an excessively refined mesh would result in unpractical computational times. The compromise solution that has been considered suitable is an element size of 0.3 x 0.3 x 0.198 mm. The considerations leading to the selection of these dimensions are discussed in Section 5.2.2.

The models have the dimensions of the real coupons with the exception of the longitudinal length. A lower longitudinal length has been chosen in order to reduce the computational time. While the length of the real coupons is 250 mm, for the FE models of the unnotched coupons a longitudinal length of 80 mm has been selected. For the open hole coupons 48 mm has been considered sufficient[16]. This reduction does not affect the prediction of the ultimate strength since only an eventual small portion of the damage area is neglected.

The use of an explicit analysis to model a quasi-static event in its natural time period leads to impractical computational times. This derives from the large number of time increments that are required to complete the simulation. By increasing the velocity imposed in the end of the coupons, the time scale of the simulations can be reduced. Thereby, fewer time increments are needed to complete the jobs [1]. Another commonly used method for obtaining an economical quasi-static solution in this type of simulation is to scale the mass. The number of increments is very large because of the small stable time increment of the analysis. The stable time increment is defined in terms of the highest element frequency in the model. For an individual element, it corresponds to the ratio between the characteristic element length L_c, and the acoustic wave speed in the material c: $\Delta t_{stable} = L_c/c$. The propagation speed of an acoustic wave is, in its simplest form, $c = \sqrt{E/\varrho}$, where E is the Young's modulus and ϱ the density of the material. Mass scaling consists on increasing the element stable time increment Δt_{stable} by artificially increasing the density ϱ [36].

In the FE models of the coupons, the load is applied by means of a velocity equivalent to 100 mm/s. The mass of the models has been scaled by a factor of 1000. Also, variable mass scaling has been used to to increase the stable time increment in the elements undergoing the largest deformations. With this, the simulation of each coupon test takes approximately 4 hours using 20 CPU's. Increasing the load rate and the mass is a generally accepted approach to reduce the computational time for simulations of quasi-static processes, provided that the induced inertial forces do not alter the solution significantly [1]. It has been confirmed with a sensitivity study that such combination of velocity and mass scaling do not introduce significant dynamic effects and only generate a negligible error in the results.

Finally, elements are deactivated (or eroded) upon reaching maximum degradation in any of the failure modes defined. In practice, this level is identified whenever a damage variable d_i reaches the value 0.999. This way, the accumulation of damage in the material is translated to a hard discontinuity in the FE model.

5.2.1 Interlaminar damage modeling

Interlaminar damage is modeled using cohesive contact surfaces between the laminas. An interface is defined between each pair of plies. The interface describes the interlaminar crack opening by allowing the introduction of discontinuities in the displacement field. In what follows, the properties of the cohesive contact surfaces implemented in the FE models are briefly presented. The type of cohesive surface adopted form part of the Abaqus/Explicit built-in library of contact interactions.

There are three pure modes leading to the initiation and propagation of an interlaminar crack. Mode I is associated to crack opening caused by a tensile stress normal to the plane of the crack. It is described by the relation between the normal component of the traction acting in the interface τ_3, and the displacement jump perpendicular to the lamina plane Δ_3. Modes II and III correspond to shear sliding and tearing respectively. The shear traction τ_1 and the relative displacement Δ_1 is associated to mode II, whilst τ_2 and Δ_2 correspond to mode III.

In the cohesive contact surface, the traction vector acting on the interface is related to the vector of displacement jumps by means of a single constitutive relation, which describes the onset and propagation of

[16] In the open hole coupons, damage is localized in the center of the specimen where the cross-sectional area is lower.

interlaminar damage in a variable mixed mode [54]: [17]

$$\begin{pmatrix}\tau_1\\ \tau_2\\ \tau_3\end{pmatrix} = (1-d)K\begin{pmatrix}\Delta_1\\ \Delta_2\\ \Delta_3\end{pmatrix} - dK\begin{pmatrix}0\\ 0\\ \langle-\Delta_3\rangle\end{pmatrix} \tag{36}$$

Damage is controlled by a single scalar damage variable d, affecting the stiffness penalty K. The stiffness penalty is the stiffness of the interface before the onset of damage. Physically, the cohesive surface should be infinitely rigid before failure initiation to represent a perfectly stiff connection between layers. Nonetheless, there has to be a finite initial stiffness to avoid numerical problems [55]. The stiffness penalty K, should be set as a compromise solution to avoid numerical undesired effects, without introducing an artificial compliance to the material. In base of the guidelines proposed by Turon et al. [55] for its definition, it has been chosen a value $K = 1 \cdot 10^6\ N/mm^3$.

Failure initiation is detected using Ye's [33] quadratic criterion. This criterion is presented in the equation 37, wherein τ_3^0, τ_2^0 and τ_1^0 are the interlaminar strengths in mode I, mode III and mode II respectively.

$$\left(\frac{\langle\tau_3\rangle}{\tau_3^0}\right)^2 + \left(\frac{\tau_2}{\tau_2^0}\right)^2 + \left(\frac{\tau_1}{\tau_1^0}\right)^2 = 1 \tag{37}$$

After failure initiation, the capacity of the interface of transferring tractions is decreased linearly. The propagation of the delamination takes place whenever the Benzeggagh-Kenane [6] criterion is met. The interlaminar crack propagates when the total energy release rate $\mathcal{G}_T = (\mathcal{G}_I + \mathcal{G}_{II} + \mathcal{G}_{III})$ reaches the mixed mode interlaminar fracture toughness $\mathcal{G}_c$, defined in equation 38, wherein $\mathcal{G}_{Ic}$ and $\mathcal{G}_{IIc}$ are the crack propagation critical ERR in mode I and II; and, $\mathcal{G}_I$, $\mathcal{G}_{II}$ and $\mathcal{G}_{III}$ are the energy release rates corresponding to modes I, II and III.

$$\mathcal{G}_c = \mathcal{G}_{Ic} + (\mathcal{G}_{IIc} - \mathcal{G}_{Ic})\left(\frac{\mathcal{G}_{II} + \mathcal{G}_{III}}{\mathcal{G}_T}\right)^\eta \tag{38}$$

Table 12 summarizes the material properties that have been used for modeling interlaminar damage with cohesive contact surfaces. The normal strength τ_3^0 of the interface has been estimated as the tensile transversal strength Y_T of the UD material system AS4-8552 [18] [24]. The interlaminar shear strength τ_1^0 is provided by the supplier [24]. The interface fracture toughness under pure mode I, and pure mode II— $\mathcal{G}_{Ic}$ and $\mathcal{G}_{IIc}$— were furnished by IMDEA Materials [19]. The mode III interlaminar strength and fracture toughness— τ_2^0 and $\mathcal{G}_{IIIc}$— have been assumed to be the same than that of mode II. The Benzeggagh-Kenane exponent η is typically obtained calibrating the equation 38 to fit experimental fracture toughness values under different mixed mode ratios [18]. In the absence of these data and pending future experimental work, it has been decided to estimate it from the literature. Values of the Benzeggagh-Kenane exponent η are usually taken in the region between 1 and 2 for UD and woven material systems [18, 30, 32]. On this basis, an exponent equal to 1.5 has been selected.

$\tau_3^0(MPa)$	$\tau_1^0(MPa)$	$\tau_2^0(MPa)$	$\mathcal{G}_{Ic}(kJ/m^2)$	$\mathcal{G}_{IIc}(kJ/m^2)$	$\mathcal{G}_{IIIc}(kJ/m^2)$	η
81	84	84	0.62	2.61	2.61	1.5

Table 12: Interlaminar strength and fracture toughness properties.

[17] In the equation 36, the use of the McCauley operator enforce that only positive normal tractions can cause mode I opening.

[18] This UD material system is constitued by the same resin and fibre than the plain weave fabric chosen for validating the model.

[19] These parameters were measured using Double Cantilever Beam (DCB) and End Notch Flexure (ENF) specimens— respectively— as part of another project.

5.2.2 Selection of the element size

This section includes the considerations that have been taken into account for selecting the size of the elements of the FE models.

Each lamina has been modeled with C3D8R brick elements. The dimension of the brick elements perpendicular to the lamina plane is fixed beforehand. It corresponds to the thickness of the plies, which is $t_p = 0.198\ mm$. The elements are squared in the plane of the lamina. For a squared-surface element, the cracking distance across the surface of the element is represented by the characteristic length defined by the following equation [5]:

$$L(\theta) = \frac{\sqrt{A_{IP}}}{\cos(\theta)} \qquad \text{with} \qquad \theta \in [0; \pi/4] \tag{39}$$

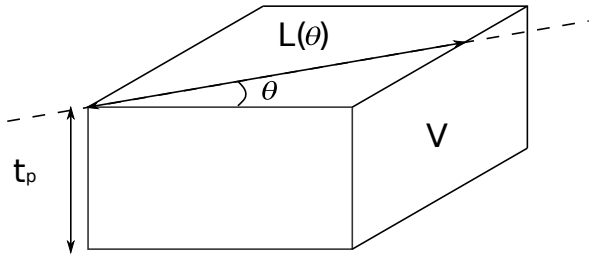

Figure 35: Definition of the characteristic element length.

wherein θ is the angle defining the orientation of the cracking direction (see Figure 35), and A_{IP} is the area associated with an integration point projected in the plane of crack propagation. For the reduced integration element with a single integration point C3D8R, the area A_{IP} coincides with the element surface $S = V/t_p$, where V is the element volume.

For an arbitrary orientation of crack propagation, the average of the function $L(\theta)$ defined in the equation 39 is usually considered [38]. Nonetheless, in the FE simulations of the coupons there is a preferred orientation at which cracks propagate: perpendicular to the loading direction. Since the mesh selected is regular and oriented at 0° with respect to the loading direction for all the ply orientations (see Figure 34), this situation corresponds to the case in which the angle of cracking direction is $\theta \approx 0°$. Accordingly, the characteristic element length that has been used in the mesh regularization scheme is the following:

$$L_c \approx \sqrt{\frac{V}{t_p}} \tag{40}$$

The election of an element size— characterized by the dimension L_c— should be a compromise solution between providing an accurate representation of the damage mechanisms and reducing the computational time.

In order to accurately represent the interlaminar crack opening mechanisms it is necessary to capture the distribution of tractions in the cohesive damage zone [54]. The size of the cohesive damage zone, is defined by a dimension known as cohesive zone length l_{cz}, which is the distance between the crack tip and the point in front of it where the traction is maximum. The size of the cohesive damage zone depends on the interlaminar failure mode. Therefore, a cohesive zone length must be defined for each mode. There are multiple cohesive zone models for estimating this length from the elasticity and strength properties of the interface [55]. They all share the same general format:

$$l_{cz} = c\ \frac{E\mathcal{G}_c}{(\tau^0)^2} \tag{41}$$

In the expression above, $\mathcal{G}_c$ is the fracture toughness and τ^0 is the interface strength, each of them specific to a given failure mode. These properties were already presented in Table 12. The constant E takes a different value depending on the failure mode as well. For the mode I, it corresponds to the modulus of the interface perpendicular to the lamina plane, which can be estimated as the transverse modulus E_2 of a UD ply with the same resin than the fabric material system. For the modes II and III, E is the shear modulus G_{12} and G_{13} of the interface, which can also be estimated as the elastic properties G_{12} and G_{13} associated to a UD ply with the same constituents than the fabric. These properties are provided by the supplier [24]. The constant c is a parameter that depends on the cohesive zone model chosen. In the absence of a cohesive zone model specific for woven fabrics, the value proposed by Hillerborg et al. [25] equal to 1.0 and commonly used for UD material systems has been adopted.

The cohesive zone lengths associated to modes I, II and III computed with the equation 41 are presented in Table 13. Mode I opening is the mode that has the lowest cohesive zone length. Therefore, this mode is in principle the one requiring the finest mesh for accurately representing the traction distribution.

l_{cz} (Mode I)	l_{cz} (Mode II)	l_{cz} (Mode III)
0.95 mm	1.85 mm	1.85 mm

Table 13: Cohesive zone length l_{cz} associated to each interlaminar mode.

Camanho et al. [10] carried out a parametric study to determine the minimum number of elements necessary to model with cohesive elements mode I opening in UD double cantilever beam specimens. They concluded that it was necessary to include at least three elements inside the cohesive zone for capturing well the traction distribution. The same value was suggested by Khoshravan [30] for glass/epoxy woven composites. The minimum number of elements that should be placed inside the cohesive zone length N_e^{min} determines the maximum size of the elements:

$$L_c^{max} = \frac{l_{cz}}{N_e^{min}} \tag{42}$$

The maximum characteristic element size necessary to reproduce with three elements mode I interlaminar damage is $L_c^{max} = 0.32\ mm$.

It should be noticed that the cohesive zone length corresponding to mode I interlaminar damage $l_{cz} = 0.95\ mm$, is approximately five times lower than the length of the process zone associated to intralaminar tensile damage $l_p = 5.0\ mm$ (see Section 4.1.1). Hence, interlaminar damage seems to be in this case more restrictive than intralaminar damage in terms of the element length necessary to model the damage mechanisms.

To recapitulate, the most restrictive failure mode in terms of the element length necessary to model the damage mechanisms is mode I interlaminar failure. In order to capture the traction distribution in front of the crack tip associated to this mode, it is required to include at least three elements in the cohesive zone. To that end, the characteristic length of the elements in the plane of the lamina must be at the most $L_c^{max} = 0.32\ mm$. Based on these considerations, it has been decided to select an element size of 0.3 x 0.3 x 0.198 mm. The characteristic element length associated to this element size is $L_c = 0.3\ mm$

Despite being the most restrictive, mode I interlaminar damage is not a very relevant failure mode in unnotched and open hole coupons under tensile loading. In that sense, mode II interlaminar damage for example plays a more important role. Consequently, element sizes slightly higher than 0.3 x 0.3 x 0.198 mm could also be used without having this a significant effect in the ultimate strength prediction of the coupons.

In the CDM model presented in Section 3.3, the fracture energy is regularized with the characteristic element length L_c for all the intralaminar failure modes (i=$\pm$1, $\pm$2, 3, 4, 5, and 6). Due to this, the larger the element is, the more steep the stiffness drop after failure initiation will be (see Figure 36). The numerical model must always at least dissipate the accumulated elastic energy. Otherwise, reproducing the snap-back behavior would be required for the model to be energy consistent. The characteristic element length above which snap-back occurs— denoted with the symbol L_c^* in Figure 36— is referred to as intralaminar critical

element length. This length can be computed for each failure mode matching the elastic strain energy at failure initiation to the fracture energy [5]:

$$L_c^* = \frac{2\ E_i G_{c\ i}}{X_i^2} \qquad where \qquad i = \pm 1, \pm 2,\ 3,\ 4,\ 5,\ 6 \tag{43}$$

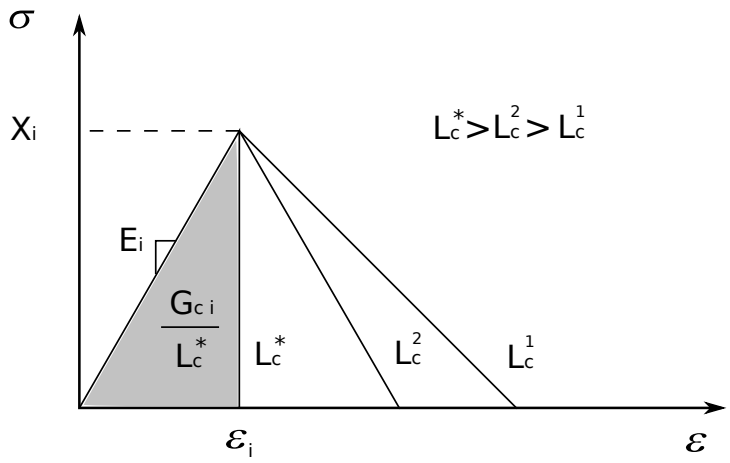

Figure 36: Fracture energy regularization and definition of the intralaminar critical element length.

The most restrictive intralaminar critical element length corresponds to the warp tensile mode, and it is equal to $L_c^* = 7.48\ mm$. In this sense, the element size chosen 0.3 x 0.3 x 0.198 mm— whose characteristic element length corresponds to $L_c = 0.3\ mm$— is way below this threshold.

5.3 Simulation results and correlation with the experimental benchmark

This section presents the results obtained with the FE models and the correlation with the experimental benchmark. In particular, the ultimate strength of the different coupons predicted with FE analysis is compared to the experimental data presented in Table 11.

In Table 14, for each coupon configuration, the ultimate strength obtained with the FE model is compared to the respective average of the strength of the experimental tests. Figure 37 shows a graphical comparison for each coupon configuration between the strength obtained with FE analysis and the corresponding average, maximum and minimum values of the experimental tests.

Specimen	Strength (Mpa)		Error %
	Average Experimental	Simulation	
UNT252	583.4	584.7	0.2
UNT181	378.6	411.4	8.7
UNT424	685.6	670.5	-2.2
OHT252	297.4	331.7	11.5
OHT181	302.6	286.4	-5.3
OHT424	349.4	326.0	-6.7

Table 14: Correlation between of ultimate strength of the coupons predicted with FE analysis against the experimental benchmark from NCAMP material database.

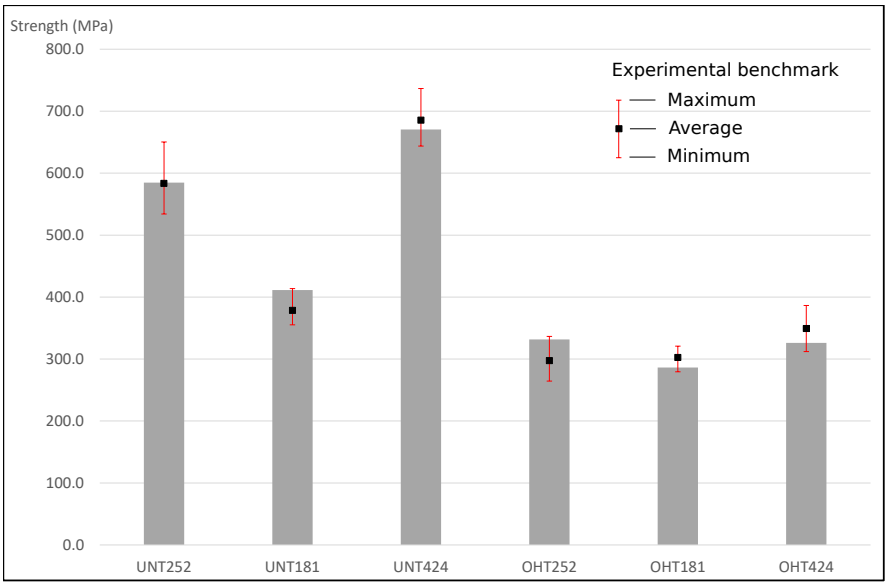

Figure 37: Graphical comparison of the strength predicted by the FE simulations of the coupons against the experimental results from NCAMP material database.

Depending on the coupon configuration, the ultimate strength predicted with FE analysis is above or below the average of the experimental tests. Predictions with an error below 3% are obtained for the coupons UNT252 and UNT424. The strength of the coupons OHT181 and OHT424 is underpredicted by less than 7%. The largest deviation from the average experimental strength is obtained for the coupons UNT181 and OHT252. In this regard, the maximum error is the one associated to the coupon configuration OHT252, corresponding to 11.5%. The prediction obtained with FE analysis is for all the coupon configurations within the maximum and minimum experimental values.

Altogether, it is reasonable to consider that with the constitutive model developed and the modeling approach described in Section 5.2 a good prediction of the ultimate strength of the coupons has been achieved.

5.4 Sensitivity study of key characteristics of the constitutive model

In this section, the relevance of the correct definition of the following features in the strength prediction of coupons under tensile loading is quantified:

(i) The shear constitutive behavior

(ii) The tensile damage law

(iii) The tensile failure criterion

For the in-plane shear constitutive behavior, it has been evaluated what is the effect in the ultimate strength of the coupons of adopting the non-linear shear behavior depicted in Section 3.1, over considering the response in shear to be linear elastic [20]. With regard to the tensile damage law, it has been assessed what is the sensitivity of the strength prediction of the coupons to the choice of the softening shape. Three damage laws have been considered for this purpose: exponential, bilinear with the input obtained from the R-curve (see Figure 28a), and bilinear with the input calibrated using the compact tension FE model (see Figure 28b). For the tensile failure criterion, it has been evaluated the effect in the strength prediction of the coupons of considering Hashin's interactive criterion expressed in equations 4 and 5 over Maximum Stress criterion.

In summary, the following comparisons have been made:

(i) Shear constitutive behavior: linear vs. non-linear

(ii) Tensile damage law: exponential vs. bilinear from R-curve vs. bilinear calibrated

(iii) Tensile failure criterion: maximum stress vs. Hashin

These comparisons have been established analyzing the strength prediction of the coupons achieved with five different CDM models. Table 15, indicates the features of these models. Hereinafter, each of the CDM models will be referred by the notation CDM X, wherein X is a number between 1 and 5. These models have different degrees of complexity, from CDM1 the simplest one, to CDM5 the one for which the results presented in the previous section were obtained.

	CDM1	CDM2	CDM3	CDM4	CDM5
Shear constitutive behavior	Linear	Non-linear	Non-linear	Non-linear	Non-linear
Tensile damage law	Exponential	Exponential	Bilinear from R-curve	Bilinear calibrated	Bilinear calibrated
Tensile failure criterion	Max. Stress	Max. Stress	Max. Stress	Max. Stress	Hashin

Table 15: Characteristics of the constitutive models used for the sensitivity study.

Table 16 depicts— for all the coupon configurations— the error of the strength prediction with respect to the experimental benchmark obtained with each of the five CDM models. In the interest of clarity, the characteristics of the CDM models have been re-stated.

[20] A linear elastic shear defined by the pristine modulus G_{12}.

	CDM1	CDM2	CDM3	CDM4	CDM5
Shear constitutive behavior	Linear	Non-linear	Non-linear	Non-linear	Non-linear
Tensile damage law	Exponential	Exponential	Bilinear from R-curve	Bilinear calibrated	Bilinear calibrated
Tensile failure criterion	Max. Stress	Max. Stress	Max. Stress	Max. Stress	Hashin
Error (%) UNT252	8.6	10.0	15.1	4.5	0.2
Error (%) UNT181	9.3	8.2	9.8	8.7	8.7
Error (%) UNT424	-1.5	-2.2	-2.1	-2.2	-2.2
Error (%) OHT252	30.3	31.0	38.3	23.1	11.5
Error (%) OHT181	5.4	4.6	6.6	4.6	-5.3
Error (%) OHT424	0.6	2.6	7.4	-4.9	-6.7

Table 16: Error in the strength prediction of the coupons achieved with different CDM models.

5.4.1 Shear constitutive behavior: linear vs. non-linear (CDM1 vs. CDM2)

In order to evaluate the effect of including the non-linear shear behavior depicted in Section 3.1 over considering the response in shear to be linear elastic, the errors in the strength predictions of the coupons obtained with the material models CDM1 and CDM2 are compared. These values can be found in Table 16.

The differences in the error of the strength prediction are, for all the coupon configurations, very small. In this regard, the maximum difference in the deviation with respect to the experimental benchmark associated to using the material model CDM2 instead of CDM1 is only 2%, corresponding to the coupon OHT424.

This evidences that, in coupons with conventional multidirectional stacking sequences complying with the 10% rule, the definition of the shear behavior is not relevant for obtaining an accurate prediction of the ultimate strength.

5.4.2 Tensile damage law: exponential vs. bilinear from R-curve vs. bilinear calibrated (CDM2 vs. CDM3 vs. CDM4)

The effect of the definition of the tensile damage law in the strength prediction of the coupons is analyzed hereafter. For this purpose, the results obtained with the material models CDM2, CDM3 and CDM4 depicted in Table 16 are compared. The damage law implemented in the constitutive model CDM2 is exponential. In the constitutive model CDM3, the damage law is the bilinear law whose input is linked to the shape of the R-curve (see Figure 28a). In the model CDM4, the damage law is the bilinear law whose input is calibrated using the FE model of the CT specimen (see Figure 28b). In the interest of clarity, these three damage laws are represented together in Figure 38.

The selection of the tensile damage law has a variable impact in the strength prediction depending on the coupon configuration. For the coupons UNT181, UNT424 and OHT181 the differences in the error of the prediction between adopting CDM2, CDM3 or CDM4 are lower than 2%. Hence, the shape of the damage law is not very relevant in those cases. On the other hand, the strength prediction of the coupons UNT252, OHT252 and OHT424 is very sensitive to the tensile damage law selected. For these coupon configurations, the steeper the tensile damage law is (see Figure 38), the lower the ultimate strength is predicted. Because of this, the strengths of UNT252, OHT252 and OHT424 predicted using the bilinear damage law calibrated with the compact tension FE model are lower than the ones obtained with the exponential damage law, which in turn are lower than the ones obtained using the bilinear damage law whose input is derived from the R-curve. Quantitatively, the difference in the strength prediction of the coupons UNT252, OHT252 and OHT424 associated to adopting the bilinear damage law parameters from the R-curve, instead of calibrating them is significant. In fact, the differences in the error are of 10.6%, 15.2% and 12.3% respectively. Therefore, the calibration of the bilinear damage law parameters is key for predicting the strength of these coupons.

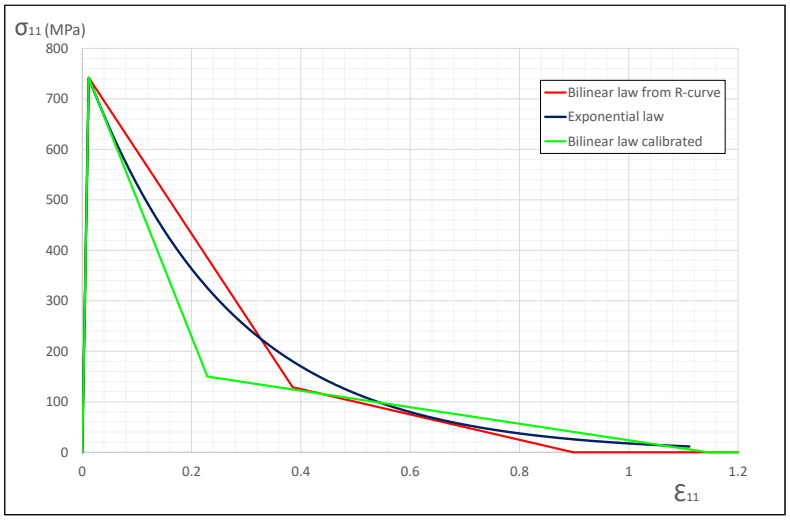

Figure 38: Comparison of different tensile damage laws

5.4.3 Tensile failure criterion: maximum stress vs. Hashin (CDM4 vs. CDM5)

The relevance of considering Hashin's failure criterion for tensile failure instead of Maximum Stress is reviewed hereafter. In the material model CDM4, the tensile failure criterion is Maximum Stress. The model CDM5 includes the Hashin's shear-tension interactive criterion that was expressed in equations 4 and 5. Figure 39, illustrates the difference between the two failure surfaces.

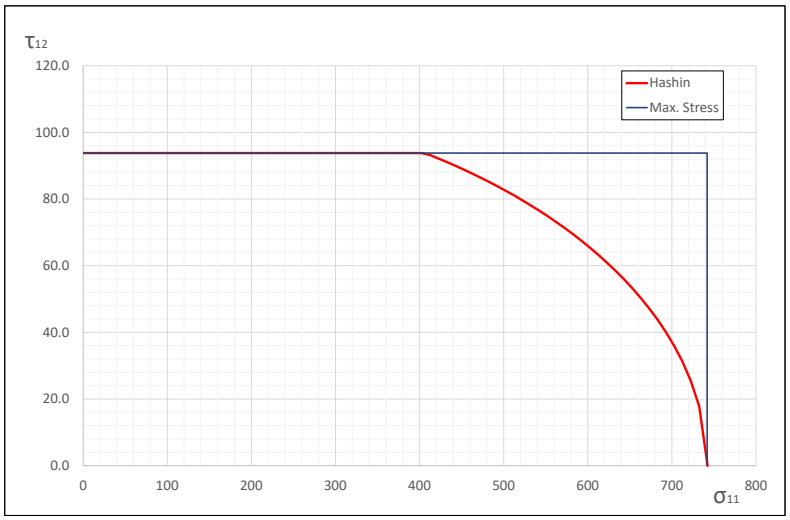

Figure 39: Hashin's and Maximum Stress failure surfaces

The deviation of the strength prediction of the coupons with respect to the experimental benchmark associated to the simulations carried out with the constitutive model CDM4 and CDM5 can be found in Table 16. It can be observed that the difference in the strength prediction caused by using CDM5 instead of CDM4 is more pronounced for the coupons with quasi-isotropic stacking sequences (252) than for the coupons with hard (424) and soft (181) laminates. Also, the open hole coupons (OHT) are more influenced than the unnotched coupons (UNT).

The reason for this is that quasi-isotropic stacking sequences and holes lead to combinations of high

tensile and shear stress in the laminates. With Hashin's failure criterion, these combinations prompt mixed mode failure at a tensile stress lower than the uniaxial allowable. An example of this situation is illustrated in Figure 40, depicting the stress field in the vicinity of the hole in a $-45°$ lamina of the coupon OHT252. It can be noticed that shear and tensile stresses concentrate simultaneously in front of the hole. As a result, tensile failure is triggered locally in mixed-mode at a strength X_T^{MMF} below X_T.

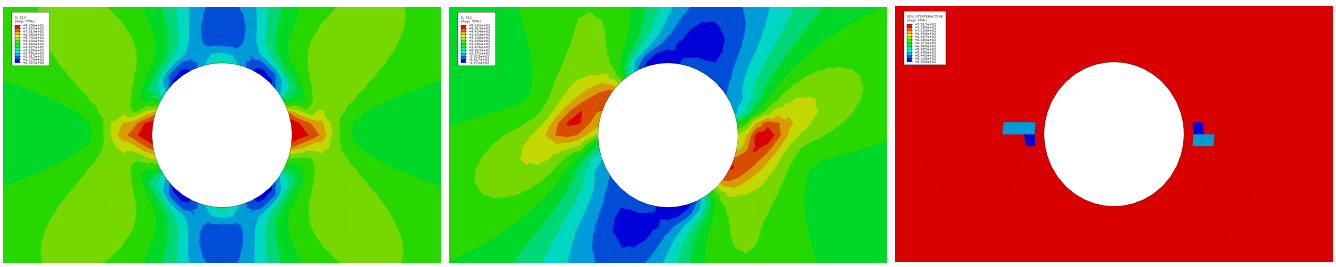

(a) Shear stress τ_{12} (b) Tensile stress σ_{11} (c) Mixed-mode strength X_T^{MMF}

Figure 40: Stress concentrations at the hole in a $-45°$ lamina of the coupon OHT252 at failure.

Differences of 11.6 % and 9.9% in the strength prediction have been found respectively for the coupons OHT252 and OHT181 associated to considering Hashin's interactive criterion over Maximum Stress. Therefore, the influence of shear stresses in the initiation and softening in the warp and weft tensile modes is a relevant aspect of the model.

5.5 Description of the failure modes of the coupons predicted with FE analysis

In this section, the failure modes of the coupons predicted with FE analysis are presented. In the absence of footage of the experimental tests, this section is merely confined to be descriptive. Future experimental work would allow to validate the failure modes against a benchmark.

Figure 41 illustrates the evolution of the damage variable d_1 in the coupon UNT252. Before the ultimate strength is reached (see Figure 41a), there is tensile damage homogeneously distributed in the laminas at $0°$ and $90°$. Progressively, the damage in these laminas starts to localize in one point at the edge. Shear and tensile damage also begins to develop in the laminas at $\pm 45°$ at the same point. The ultimate strength is reached when the localized damage exceeds a certain level (see Figure 41b). The crack generated at the edge propagates transversely in the laminas at $0°$ and $90°$, causing the load to be transferred to the laminas with orientation $\pm 45°$. These, in turn accumulate shear and tensile damage locally and end up failing as well (see Figure 41c).

The failure mode predicted of the coupon UNT181 is illustrated in Figure 42. Before reaching the ultimate strength, the laminas with orientations $0°$ and $90°$ accumulate tensile damage. Figure 42a depicts how the tensile damage is distributed. Progressively, the tensile damage in the laminas at $0°$ and $90°$ starts to concentrate in two bands of elements at $45°$. At the stage depicted in Figure 42b the ultimate strength of the coupon is reached, corresponding to the brittle fracture of the laminas at $0°$ and $90°$ along the two bands. These laminas represent however only 20% of the laminate. Therefore, after reaching the ultimate strength of the coupon, the laminas at $\pm 45°$ are still able to carry load. A residual load is maintained while the laminas continue accumulating shear and tensile damage (see Figure 42c), before the coupon eventually collapses.

It should be recalled that the characteristic element length L_c used in the mesh regularization scheme was computed assuming that the preferred orientation of the crack propagation was perpendicular to the loading direction. For the coupon UNT181, the failure bands are, however, aligned at $45°$. Which means that the fracture toughness per characteristic element length L_c in the elements of these bands is being overestimated. This may be one of the reasons causing the strength prediction for this specific coupon to be 8.7% higher than the average of the experimental tests. A practical solution to mitigate this effect would be to orient the mesh at $45°$ for all the plies of this coupon.

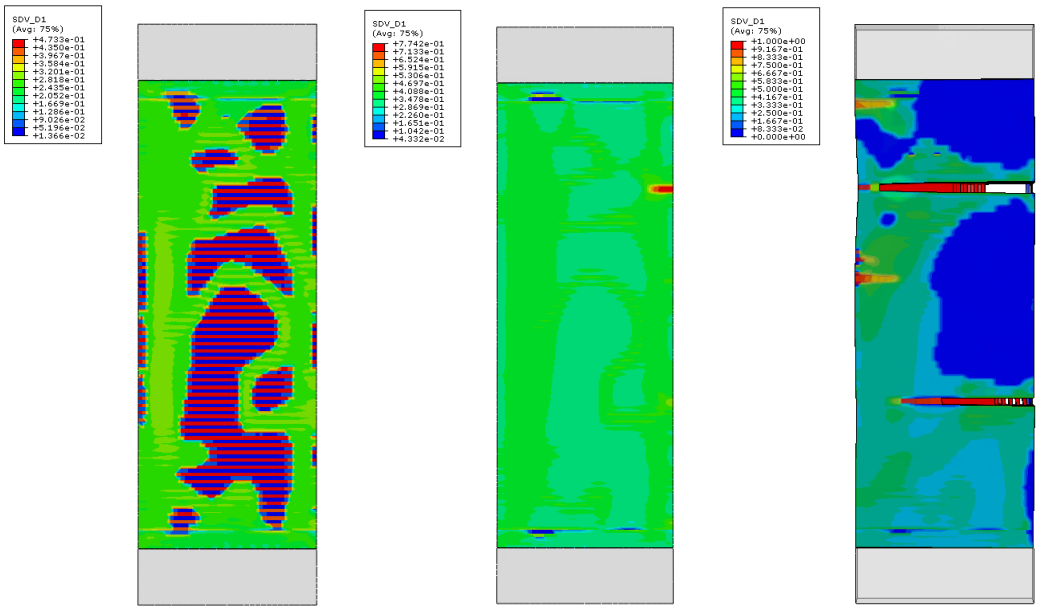

(a) Before ultimate strength: d_1 (b) At ultimate strength: d_1 (c) After ultimate strength: d_1

Figure 41: Failure mode of the coupon UNT252. Translucency: On.

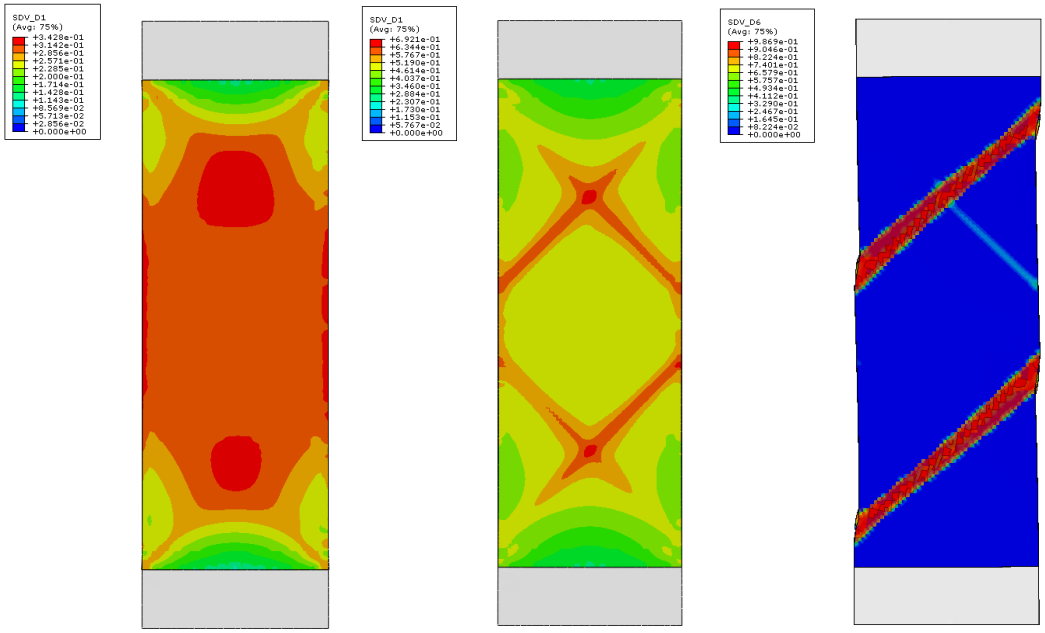

(a) Before ultimate strength: d_1 (b) At ultimate strength: d_1 (c) After ultimate strength: d_6

Figure 42: Failure mode of the coupon UNT181. Translucency: On.

Figure 43 shows the evolution of the damage variable d_1 in the coupon UNT424. The failure of this specimen is very brittle. In this respect, as soon as tensile damage in the laminas with orientations 0° and

90° is prompted, the ultimate strength is reached. This can explain the fact that the prediction of the ultimate strength of this coupon does not depend on which tensile damage law is chosen (see Section 5.4.2). After initiation has taken place, the damage continues to develop resulting in the formation of cracks aligned in the transverse direction. These cracks rapidly propagate and the laminate looses entirely its capacity to withstand load.

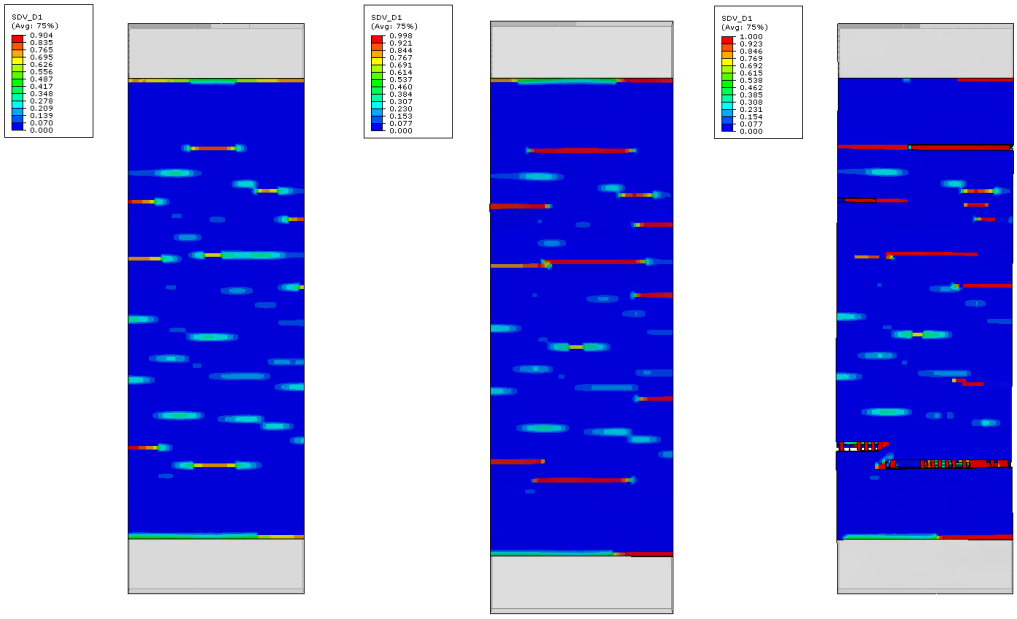

(a) At ultimate strength (b) After ultimate strength (1) (c) After ultimate strength (2)

Figure 43: Failure mode of the coupon UNT424. Translucency: On. Ploted: Damage variable d_1.

The failure mode of the open hole coupon OHT252 obtained with FE analysis is detailed next. Figures 44 and 45 display the evolution of the damage variables d_1 and d_6 respectively. In the laminas at 0° and 90°, the stress concentration around the hole promotes tensile damage, whereas in the laminas at ±45°, there is a combination of high shear and tension stresses (see Figure 40) prompting tension and shear damage simultaneously. The damage, exclusively localized in the region with the lowest cross sectional area, propagates transversely. The laminas at 0° and 90° are the first to fail completely, followed by the ones with orientation ±45°.

The failure modes obtained with FE analysis of the open hole coupons OHT181 and OHT424 are very similar to the one of OHT252. The evolution of the damage variables d_1 and d_6 in these specimens can be consulted in Annex C.

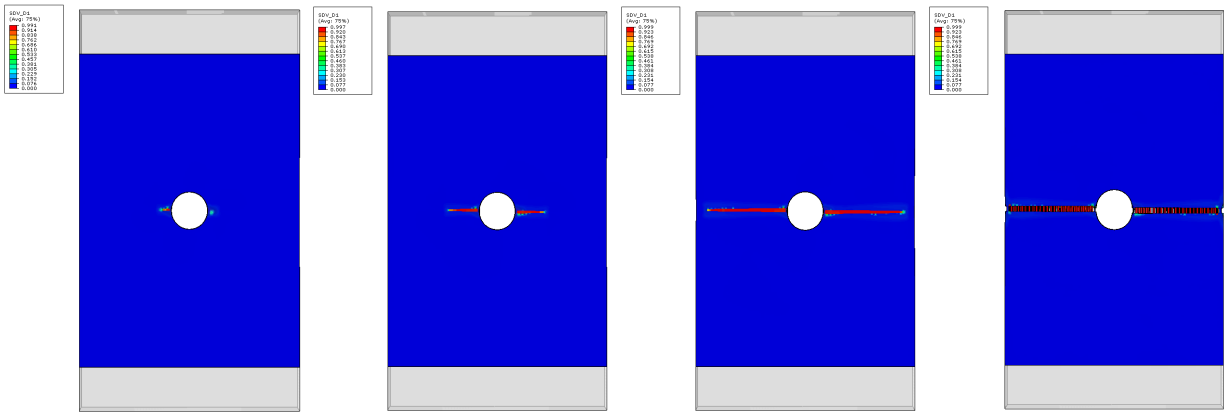

Figure 44: Evolution of the damage variable d_1 on the coupon OHT252. Translucency: On.

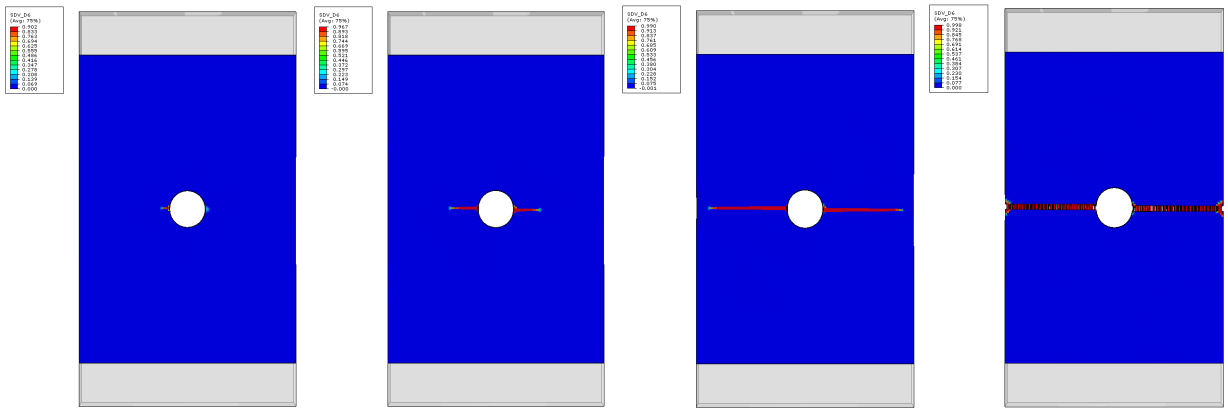

Figure 45: Evolution of the damage variable d_6 on the coupon OHT252. Translucency: On.

5.6 Reproduction of the in-plane shear test

In the current implementation, Ramberg-Osgood law is used to reproduce the shear constitutive behavior (see equation 2). In Section 4.2.1 it has been depicted how this expression has been calibrated so that it matches with the shear stress-strain response obtained from tensile testing of a $[\pm 45]_{3s}$ coupon. Implicitly, it has been assumed that the shear response at the constitutive level corresponds to the one measured at coupon level. There are reasons to think that this may not entirely be true. For example, other damage mechanisms may be involved in the non-linear response measured.

With the objective of evaluating the difference between the shear response at the constitutive level and the one at coupon level, it has been decided to reproduce the test of the $[\pm 45]_{3s}$ coupon with a FE simulation. The same modeling approach that was presented in Section 5.2, has been followed to build the FE model.

Figure 46 presents: (i) the shear stress-strain response obtained experimentally from the tensile test of the $[\pm 45]_{3s}$ coupon, (ii) the fit of the aforementioned experimental curve that is implemented at the constitutive level, and (iii) the shear stress-strain response obtained with the FE simulation of the $[\pm 45]_{3s}$ coupon.

It can be noticed, a mismatch between the response at the constitutive level and the one obtained with the FE simulation. The difference between the curves becomes only apparent for shear strains higher than 5%, and gradually increases. For a shear strain corresponding to 10%, the mismatch is of 5.5%. These observations highlight that the shear constitutive behavior is not completely well reproduced at high strains because coupon related effects are being neglected.

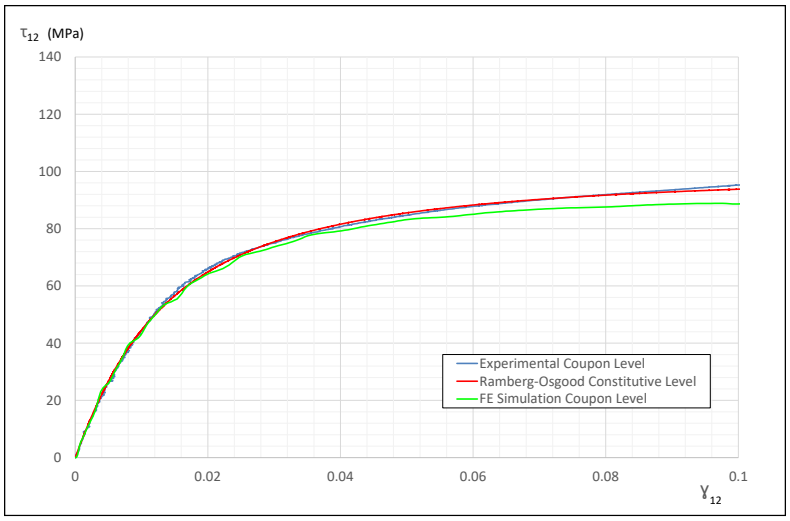

Figure 46: Comparison of the shear stress-strain response obtained with the FE model of a $[\pm 45]_{3s}$ coupon against the response implemented at constitutive level.

Nonetheless, as was shown in Section 5.4.1, the correct definition of the shear behavior is not relevant for obtaining an accurate prediction of the ultimate strength of coupons with stacking sequences complying with the 10% design rule. This is even more conspicuous when the part of the shear constitutive model that is not reproduced correctly corresponds to the response for high shear strains.

5.7 Conclusions

The proposed constitutive model has been used in a set of FE simulations of unnotched and open hole coupons under quasi-static tensile loading conditions. The ultimate strength predicted with FE analysis was compared to a benchmark of experimental results for different multistacking sequences.

The maximum deviation reported between the prediction obtained with FE analysis and the experimental average amounts to 11.5%, corresponding to the simulation of the coupon OHT252. For all the coupon configurations, the prediction obtained with FE analysis lays between the maximum and minimum experimental values. In view of this, it has been concluded that a reasonably good correlation to the experimental data has been achieved.

A sensitivity study was carried out to assess the relevance of the three "key" characteristics of the constitutive model in the strength prediction of the coupons, namely: the shear constitutive behavior, the tensile damage law, and the tensile failure criterion. From this study, it was concluded that the definition of the shear behavior is not relevant for obtaining an accurate prediction of the ultimate strength of coupons complying with the 10% rule. On the other hand, the proper calibration of the tensile damage law was found to be an essential aspect for obtaining a good prediction of the ultimate strength for some coupon configurations. Similarly, including the interaction of shear stresses in the initiation and propagation of damage in tension has a great impact in the strength prediction of the coupons wherein combinations of high tensile and shear stresses develop in the plies.

The failure modes obtained with FE analysis were examined in detail. In particular, the accumulation of intralamnar damage leading to the collapse of the coupons was characterized in order to provide a better understanding of the ultimate strengths reported.

Finally, the off-axis tensile test of the $[\pm 45]_{3s}$ laminate whose results were presented in Section 4.2.1 was reproduced with a FE simulation. The purpose was to evaluate the difference between the shear response at the constitutive level and the one at coupon level. Small differences were found for shear strains higher than 5%. However, these differences were considered to be inconsequential for the objective of this work.

6 Conclusions and future work

6.1 Conclusions

A novel continuum damage mechanics model for 2D woven fabrics has been developed and implemented in a VUMAT subroutine for Abaqus/Explicit. The model takes into account the shear non-linearity caused by the accumulation of damage and plasticity in the matrix, the toughening mechanisms in the tensile failure mode, and the in-plane shear to tension mode mixity.

The shear non-linear constitutive relation was reproduced adopting the Ramberg-Osgood law, which was fitted using as physical reference the results obtained from the experimental tensile test of ± 45 off-axis coupons. Cyclic in-plane shear tests were carried out to characterize the effect of the accumulation of damage in the matrix caused by shear loading. The proposed constitutive model for shear, takes into account the permanent deformation and the degradation of the secant modulus.

A bilinear damage law was proposed to account for the toughening mechanisms associated to tensile failure. The damage law was formulated such that its input could be determined from the shape of the R-curve measured with CT specimens. However, it was discovered that this methodology is not suitable for woven composites. Essentially, it was found that the critical energy release rate that the elements should display after failure initiation to reproduce the crack opening does not correspond to the resistance curve measured with CT tests. This mismatch was attributed to the homogenization of the fabric properties. To circumvent this problem, an engineering solution consisting on calibrating the bilinear damage law with a FE model of the CT test was proposed.

Based on the analysis of fractography found in the literature, it was noticed that the matrix damage caused by shear loading interacts with the warp and weft tensile modes. In order to take into account this interaction, it was proposed to use Hashin's quadratic criterion for predicting tensile failure initiation. The effect of the damage caused by shear loading in the propagation of tensile cracks was included by scaling the damage law proportionally to the degree of mode mixity.

The constitutive model was validated by comparing the results of finite element predictions with experimental data from unnotched and open hole specimens with different multistacking sequences under quasi-static tensile loading conditions. A good correlation was achieved between the prediction of the ultimate strength of the coupons and the experimental results.

6.2 Suggestions for future work

There are several aspects of the CDM model proposed that need further investigation before it can be routinely used to predict progressive failure in woven composites.

The shape of the failure envelope associated to the tensile failure criterion is yet to be validated. In this interest, an experimental shear-tension failure surface could be obtained by testing coupons with different off-axis angles. The results could be then compared to the proposed level of interaction. Another aspect worth to investigate is to which point the failure modes predicted of the coupons correlate with the experimental ones. This could be useful in order to identify potential limitations in the application for 2D woven composites of the homogenized CDM modeling approach. Further work must also be carried out to assess the validity of applying the constitutive model proposed to material systems with different tow interlacing architectures than plain weave.

Modeling interlaminar failure of woven laminates with cohesive contact surfaces entails additional challenges not present in UD composites that have not been addressed in this work. Woven material systems display higher fracture toughnesses than their UD counterparts in mode I and mode II. This is mainly because the propagation of the delaminations in woven composites is hindered by the tow architecture, resulting in a tortuous crack path. Because of this, the homogenized fracture toughnesses in mode I and mode II do not correspond to the local critical energy release rate of the interface. This mismatch is not taken into account in the present model and may be introducing non-negligible errors in the strength prediction of the coupons, wherein interlaminar damage plays an important role in the initiation of cracks at the free edges. An engineering solution to this problem could be to calibrate the traction-separation laws associated

to mode I and mode II by matching the response of Double Cantilever Beam and the End Notch Flexure tests with FE models integrating the cohesive contact surfaces.

Future research has to be done also regarding how to include in macroscale CDM models for woven composites the onset and propagation of damage in compression. Kink-band formation is the predominant failure mechanism for compressive loaded woven composites. A phenomenological criterion for kink-band initiation in woven fabrics is yet to be developed. The difficulty of this lies in that the mechanisms leading to the initiation of kink-bands take place at meso and micro scale level and are heavily dependent on the tow architecture. A suitable softening law for describing the kink-band propagation also needs to be proposed. In the spirit of the work performed by Catalanotti [11], it is suggested to define the damage law in compression based on a size effect law obtained by testing a set of double-edge notched specimens with different widths.

References

[1] ABAQUS online documentation. Analysis user's manual 11.6.1. SIMULIA Inc. Dassault Systems, 2016.

[2] ASTM. Standard Test Method for Plane-Strain Fracture Toughness of Metallic Materials. E 399. Technical report, 1997.

[3] ASTM. Standard Test Method for Open Hole Tensile Strength of Polymer Matrix Composite Laminates. D 5766. Technical report, 2002.

[4] ASTM. Standard Test Method for In-Plane Shear Response of Polymer Matrix Composite Materials by Tensile Test. D 3518/D 3518M. Technical report, 2007.

[5] Z Bazant and B Oh. Crack band theory of concrete. *Materials and Structures*, 16:155–177, 1983.

[6] M. L. Benzeggagh and M. Kenane. Measurement of mixed-mode delamination fracture toughness of unidirectional glass/epoxy composites with mixed-mode bending apparatus. *Composites Science and Technology*, 56(4):439–449, 1996.

[7] N. Blanco, D. Trias, S. T. Pinho, and P. Robinson. Intralaminar fracture toughness characterisation of woven composite laminates. Part I: Design and analysis of a compact tension (CT) specimen. *Engineering Fracture Mechanics*, 131:349–360, 2014.

[8] N. Blanco, D. Trias, S. T. Pinho, and P. Robinson. Intralaminar fracture toughness characterisation of woven composite laminates. Part II: Experimental characterisation. *Engineering Fracture Mechanics*, 131:361–370, 2014.

[9] Travis A. Bogetti, Christopher P R Hoppel, Vasyl M. Harik, James F. Newill, and Bruce P. Burns. Predicting the nonlinear response and progressive failure of composite laminates. *Failure Criteria in Fibre-Reinforced-Polymer Composites*, 64:402–428, 2004.

[10] P. Camanho and C.G. Davila. Mixed-Mode Decohesion Finite Elements in for the Simulation Composite of Delamination Materials. *Nasa*, TM-2002-21(June):1–37, 2002.

[11] G. Catalanotti, J. Xavier, and P. P. Camanho. Measurement of the compressive crack resistance curve of composites using the size effect law. *Composites Part A: Applied Science and Manufacturing*, 56(January):300–307, 2014.

[12] Olivier Cousigné, David Moncayo, Daniel Coutellier, Pedro Camanho, and Hakim Naceur. Numerical modeling of nonlinearity, plasticity and damage in CFRP-woven composites for crash simulations. *Composite Structures*, 115(1):75–88, 2014.

[13] Olivier Cousigné, David Moncayo, Daniel Coutellier, Pedro Camanho, Hakim Naceur, and Steffen Hampel. Development of a new nonlinear numerical material model for woven composite materials accounting for permanent deformation and damage. *Composite Structures*, 106:601–614, 2013.

[14] Brian N. Cox and Gerry Flanagan. Handbook Composites of Analytical Methods for Textile. *NASA Contractor Report*, (March 1997):176, 1997.

[15] Carlos G. Davila, Pedro P. Camanho, and Cheryl A. Rose. Failure Criteria for FRP Laminates. *Journal of Composite Materials*, 39(4):323 – 345, 2005.

[16] Carlos G Dávila and Cheryl A Rose. Superposition of Cohesive Elements to Account for R-Curve Toughening in the Fracture of Composites. *2008 Abaqus Users' Conference*, pages 1–15, 2008.

[17] M V Donadon and S F M de Almeida. *2.07 - Damage Modeling in Composite Structures*, volume 2. Elsevier, 2014.

[18] O. Falco, C. S. Lopes, F. Naya, F. Sket, P. Maimi, and J. A. Mayugo. Modelling and simulation of tow-drop effects arising from the manufacturing of steered-fibre composites. *Composites Part A: Applied Science and Manufacturing*, 93:59–71, 2017.

[19] A. Garcia-Carpintero, B. Van den Beuken, S. Haldar, M. Herraez, C. S. Lopes, and C. Gonzalez. Fracture behaviour of triaxial braided composites and its simulation using multi-material shell modeling approach. *Submitted to Engineering Fracture Mechanics*, pages 1–35, 2017.

[20] Emile S. Greenhalgh. The influence of fibre architecture in the failure of polymer composites. In *Failure Analysis and Fractography of Polymer Composites*, chapter 6, pages 279–355. Woodhead, 2009.

[21] R. Gutkin, M. L. Laffan, S. T. Pinho, P. Robinson, and P. T. Curtis. Modelling the R-curve effect and its specimen-dependence. *International Journal of Solids and Structures*, 48(11-12):1767–1777, 2011.

[22] H. T. Hahn and S. W. Tsai. Nonlinear Elastic Behavior of Unidirectional Composite Laminae. *Journal of Composite Materials*, 7(January 1973):102–118, 1973.

[23] Z. Hashin. Failure Criteria for Unidirectional Fiber Composites. *Journal of Applied Mechanics*, 47(2):329, 1980.

[24] Hexcel Composites. Product data HexPly 8552. *Hexcel*, pages 1–6, 2000.

[25] A Hillerborg, M Modeer, and Petersson. Analysis of crack formation and crack growth in concrete by means of fracture mechanics and finite elements. *Cement and Concrete Research*, 6:773–782, 1976.

[26] Ch Hochard, P. A. Aubourg, and J. P. Charles. Modelling of the mechanical behaviour of woven-fabric CFRP laminates up to failure. *Composites Science and Technology*, 61(2):221–230, 2001.

[27] David R. Hufner and Michael L. Accorsi. A progressive failure theory for woven polymer-based composites subjected to dynamic loading. *Composite Structures*, 89(2):177–185, 2009.

[28] L. Iannucci. Progressive failure modelling of woven carbon composite under impact. *International Journal of Impact Engineering*, 32(6):1013–1043, 2006.

[29] Masoud Haghi Kashani and Abbas S Milani. Damage Prediction in Woven and Non-woven Fabric Composites. In *Non-woven Fabrics*, chapter 10. 2016.

[30] M Khoshravan. Cohesive Zone Parameters Selection for Mode-I Prediction of Interfacial Delamination. 61:507–516, 2015.

[31] M. J. Laffan, S. T. Pinho, P. Robinson, and L. Iannucci. Measurement of the in situ ply fracture toughness associated with mode I fibre tensile failure in FRP. Part I: Data reduction. *Composites Science and Technology*, 70(4):606–613, 2010.

[32] Frank a Leone, Structural Mechanics, and Concepts Branch. Representing Matrix Cracks Through Decomposition of the Deformation Gradient Tensor in Continuum Damage Mechanics Methods. (July):19–24, 2015.

[33] Lin Ye. Role of matrix resin in delamination onset and growth in composite laminates. *Composites Science and Technology*, 33(4):257–277, 1988.

[34] Teddy Lisle, Christophe Bouvet, Marie-Laetitia Pastor, Thomas Rouault, and Philippe Margueres. Damage of woven composite under tensile and shear stress using infrared thermography and micrographic cuts. *Journal of materials science*, 50(18):6154–6170, 2015.

[35] Kuo Shih Liu and Stephen W. Tsai. A progressive quadratic failure criterion for a laminate. *Composites Science and Technology*, 58(7):1023–1032, 1998.

[36] Claudio Saul Lopes. *Damage and Failure of Non-Conventional Composite Laminates*. PhD thesis, TU Delft, 2009.

[37] P. Maimí, P. P. Camanho, J. A. Mayugo, and C. G. Dávila. A continuum damage model for composite laminates: Part I - Constitutive model. *Mechanics of Materials*, 39(10):897–908, 2007.

[38] P. Maimí, P. P. Camanho, J. A. Mayugo, and C. G. Dávila. A continuum damage model for composite laminates: Part II - Computational implementation and validation. *Mechanics of Materials*, 39(10):909–919, 2007.

[39] Pere Maimí, Pedro P Camanho, Joan Andreu Mayugo, and Carlos G Dávila. A Thermodynamically Consistent Damage Model for Advanced Composites. NASA/TM-2006-214282. *Nasa Tm*, (March):47, 2006.

[40] E. Martín-Santos, P. Maimí, E. V. González, and P. Cruz. A continuum constitutive model for the simulation of fabric-reinforced composites. *Composite Structures*, 111(1):122–129, 2014.

[41] IMDEA Materials. Crashing characterization of structural behavior for high frequency phenomena. Technical report.

[42] R. Muñoz, F. Martínez-Hergueta, F. Gálvez, C. González, and J. LLorca. Ballistic performance of hybrid 3D woven composites: Experiments and simulations. *Composite Structures*, 127:141–151, 2015.

[43] M. Naik, N., Shembekar, P., and Hosur. Failure Behavior of Woven Fabric Composites. *Journal of Composites, Technology and Research*, 13(2):107–116, 1991.

[44] NASA Langley Research Center. Composite Damage (CompDam) Progressive Damage Analysis Software, 2017.

[45] NCAMP. Hexcel 8552S AS4 Plain Weave Fabric Prepreg 193 gsm. Technical report, 2011.

[46] Shinji Ogihara and Kenneth L. Reifsnider. Characterization of nonlinear behavior in woven composite laminates. *Applied Composite Materials*, 9(4):249–263, 2002.

[47] Federico Paris and Karen E Jackson. A Study of Failure Criteria of Fibrous Composite Materials. Technical Report March, 2001.

[48] S T Pinho, P Robinson, and L Iannucci. Fracture toughness of the tensile and compressive fibre failure modes in laminated composites. *Preprint submitted to Elsevier Science*, (December 2005), 2006.

[49] A. Puck and H. Schürmann. Failure Analysis of Frp Laminates By Means of Physically Based Phenomenological Models. *Composites Science and Technology*, 58(7):1045–1067, 1998.

[50] S. Silvestre Pinho R. Gutkin, , N. V. De Carvalho Pimenta, and P. Robinson. Fibre-dominated compressive failure in polymer matrix composites. In *Failure mechanisms in polymer matrix composites Criteria, testing and industrial applications*, chapter 7, pages 183–213. Woodhead, 2012.

[51] Cheryl a Rose, Carlos G Dávila, and Frank a Leone. Analysis Methods for Progressive Damage of Composite Structures. (July):48, 2013.

[52] C.T. Sun and J.L. Chen. A Simple Flow Rule for Characterizing Nonlinear Behavior of Fiber Composites. *Journal of Composite Materials*, 23(10):1009–1020, 1989.

[53] Wei Tan and Brian G. Falzon. Modelling the nonlinear behaviour and fracture process of AS4/PEKK thermoplastic composite under shear loading. *Composites Science and Technology*, 126:60–77, 2016.

[54] Albert Turon Traversa. *Simulation of delamination in composites under quasi-static and fatigue loading using cohesive zone models*. PhD thesis, UdG, 2006.

[55] A Turon, C.G. Davila, P P Camanho, and J Costa. An engineering solution for mesh size effects in the simulation of delamination using cohesive zone models. 74:1665–1682, 2007.

[56] W. Van Paepegem, I. De Baere, and J. Degrieck. Modelling the nonlinear shear stress-strain response of glass fibre-reinforced composites. Part I: Experimental results. *Composites Science and Technology*, 66(10):1455–1464, 2006.

[57] J. S. Welsh. Comparison of MCT Failure Prediction Techniques and Experimental Verification for Biaxially Loaded Glass Fabric-reinforced Composite Laminates. *Journal of Composite Materials*, 38(24):2165–2181, 2004.

Appendix A Load-reversal cyclic in-plane shear

In order to ensure the consistency of the model, it is necessary to define the response of the material for all the potential loading cases, even the ones that are unlikely to happen. Particularly, due to the implementation of a non-linear shear response, it has to be addressed the case of shear cyclic loading with load-reversal.

For simplicity, the damage and plasticity generated by shear loading have been considered to be orientationally invariant. This implies that, in the circumstance of reloading in shear with opposite sign after fully unloading, the material should resume the accumulation of damage and plasticity from the level where unloading began. For this purpose, the shear constitutive model has been generalized for a case in which i unloading phases are followed by loading phases of opposite sign.

The accumulation of damage and plasticity is tracked in the numerical model storing the strains corresponding to the transition from loading to unloading (γ_{12}^{unl}) and from unloading to reloading (γ_{12}^{rel}). From this, and the current shear strain, it is possible to compute the historical shear strain generated during the loading phases after i unloading phases have taken place. This strain, hereinafter referred as cumulative shear strain, is defined as:

$$\tilde{\gamma_{12}}^{i}(\gamma_{12}) = \gamma_{12} + sign(\gamma_{12}) \left[\sum_{1}^{i} |\gamma_{12_i}^{unl}| - \sum_{1}^{i} |\gamma_{12_i}^{rel}| \right] \tag{44}$$

Loading in shear after i unloadings takes place following the Ramberg-Osgood expression depicted in equation 45; wherein, with regard to equation 2, the strain γ_{12} has been replaced by the cumulative strain $\tilde{\gamma_{12}}^{i}$. By the same token, the equation 3 has been generalized to comprehend this situation. The expression 46 shows the resulting formulation. Figure 47 illustrates the cyclic shear constitutive behavior before failure initiation associated to these two expressions.

$$\text{Loading:} \qquad \hat{\tau_{12}} = \frac{G_{12}\ \tilde{\gamma_{12}}^{i}(\gamma_{12})}{\left(1 + \left(\frac{G_{12}\ |\tilde{\gamma_{12}}^{i}(\gamma_{12})|}{\tau_{12}^{a}}\right)^{\rho}\right)^{1/\rho}} \tag{45}$$

$$\text{Unloading:} \qquad \hat{\tau_{12}} = G_{12}^{*}(\tilde{\gamma_{12}}^{i}(\gamma_{12_{i+1}}^{unl}))\Big[\gamma_{12} - \gamma_{12p}(\tilde{\gamma_{12}}^{i}(\gamma_{12_{i+1}}^{unl}))\Big] \tag{46}$$

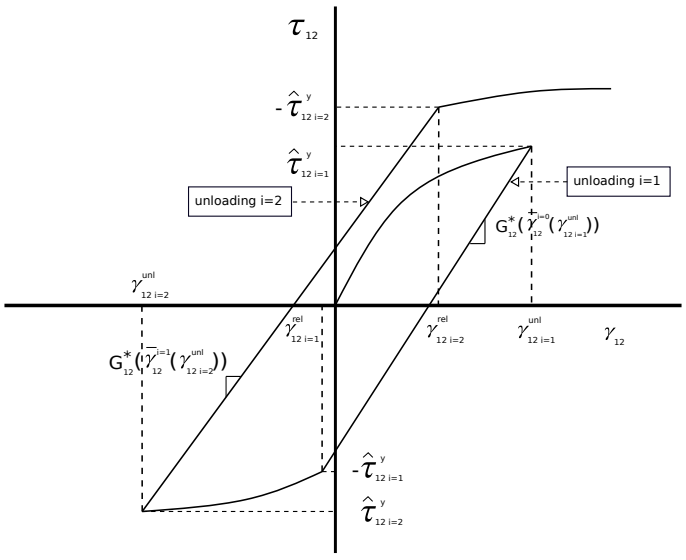

Figure 47: Load-reversal cyclic in-plane shear before failure initiation

After failure initiation, softening and unloading in shear is described by the equation 47. As in the previous cases, with regard to equation 10, the shear strain γ_{12} has been replaced by the cumulative strain $\tilde{\gamma_{12}}^{i}$. The response that the constitutive model yields in case of cyclic shear loading after failure initiation is depicted in Figure 48.

$$\tau_{12} = G^{*}_{12}(\tilde{\gamma_{12}}^{i}(\gamma^{0}_{12}))\Big[1 - d_6\Big]\Big[\gamma_{12} - \gamma_{12p}(\tilde{\gamma_{12}}^{i}(\gamma^{0}_{12}))\Big] \tag{47}$$

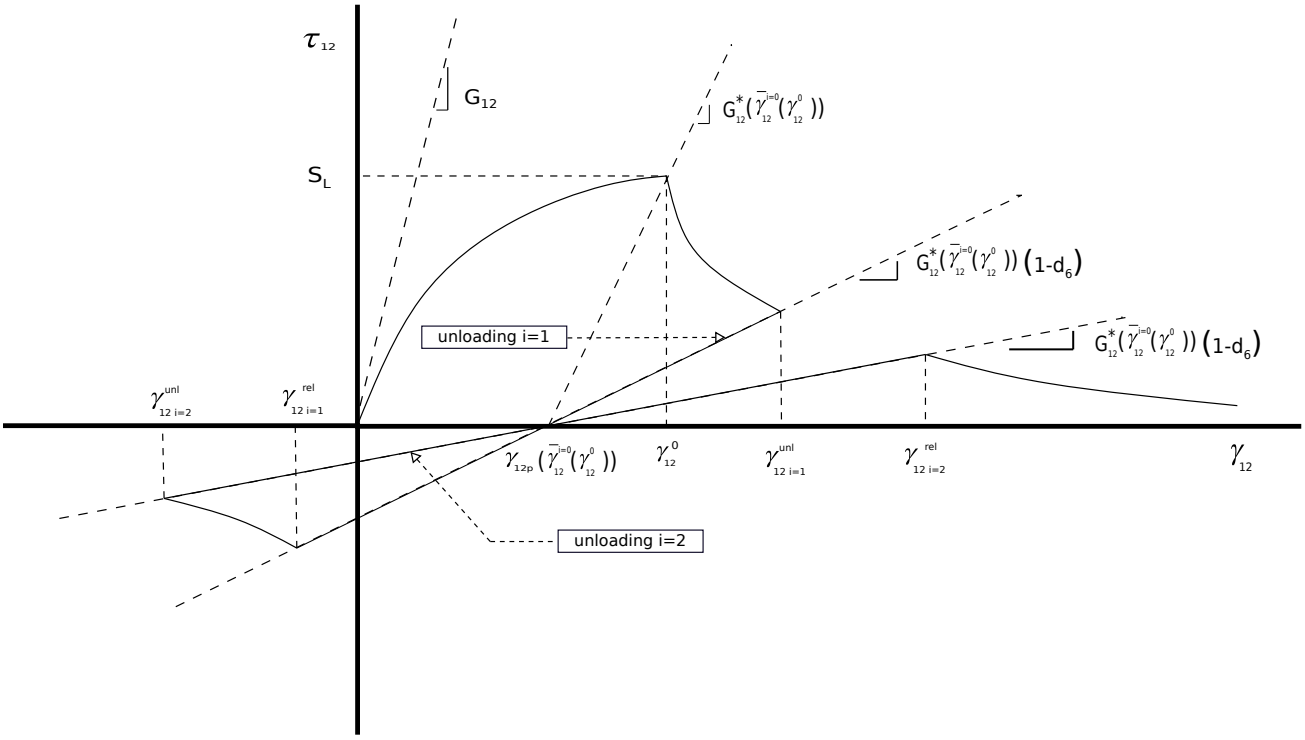

Figure 48: Load-reversal cyclic in-plane shear after failure initiation

Appendix B Experimental cyclic shear stress vs. strain curves

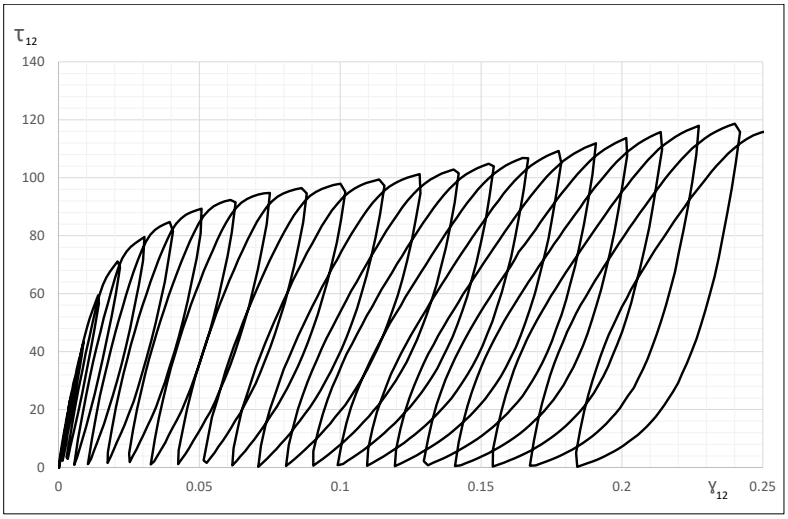

Figure 49: Cyclic in-plane shear test stress-strain curve of a $[\pm 45^\circ]_{3s}$ laminate. Specimen 1.

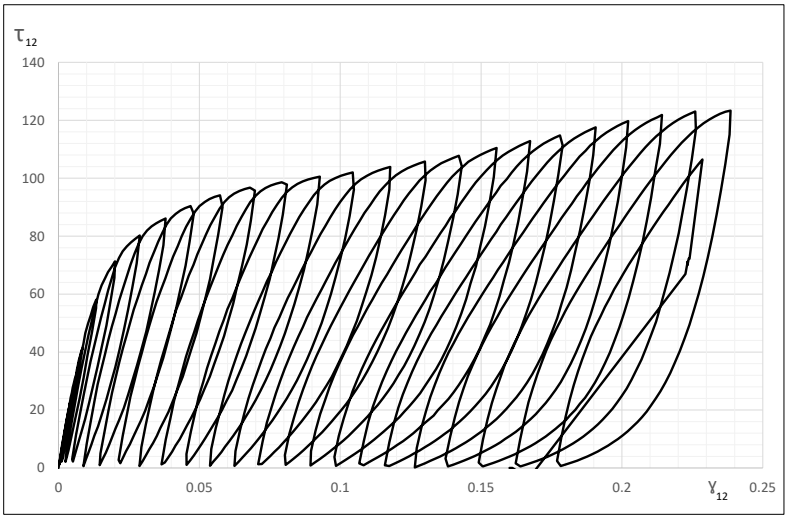

Figure 50: Cyclic in-plane shear test stress-strain curve of a $[\pm 45^\circ]_{3s}$ laminate. Specimen 2.

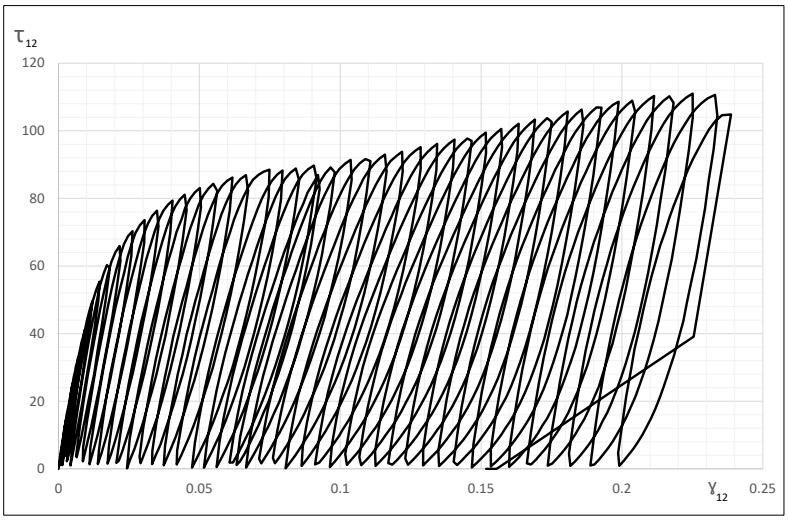

Figure 51: Cyclic in-plane shear test stress-strain curve of a $[\pm 45^\circ]_{3s}$ laminate. Specimen 3.

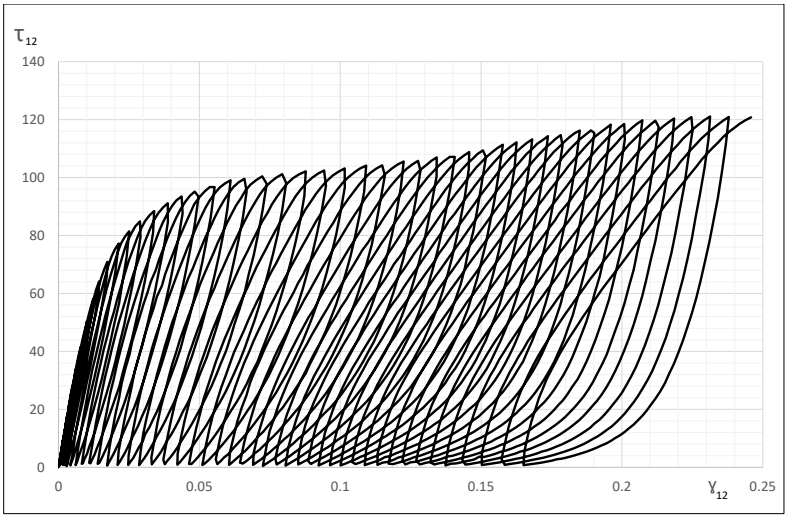

Figure 52: Cyclic in-plane shear test stress-strain curve of a $[\pm 45^\circ]_{3s}$ laminate. Specimen 4.

Appendix C Failure modes predicted by FE analysis of the coupons OHT181 and OHT424

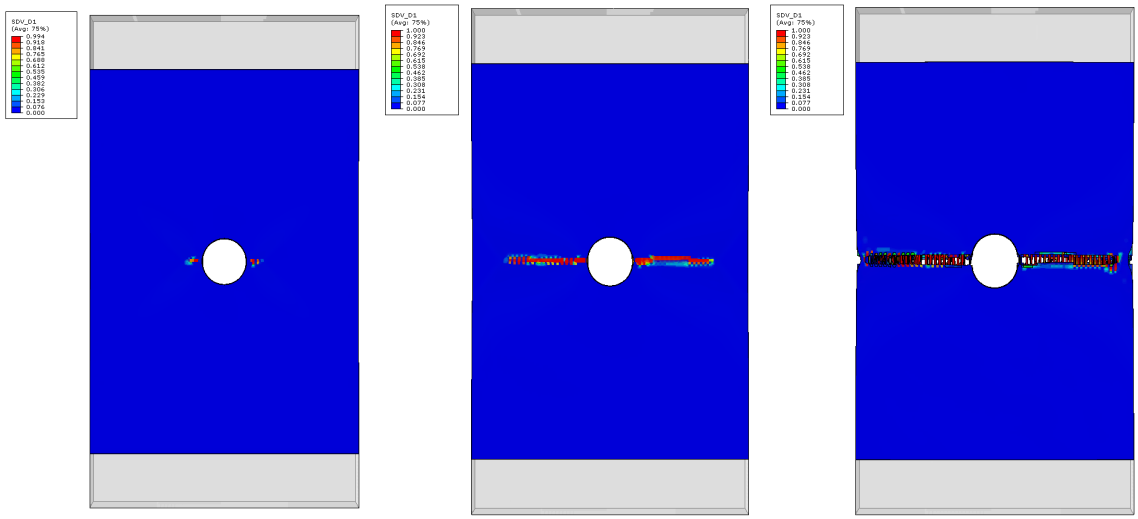

Figure 53: Evolution of the damage variable d_1 on the coupon OHT181. Translucency: On.

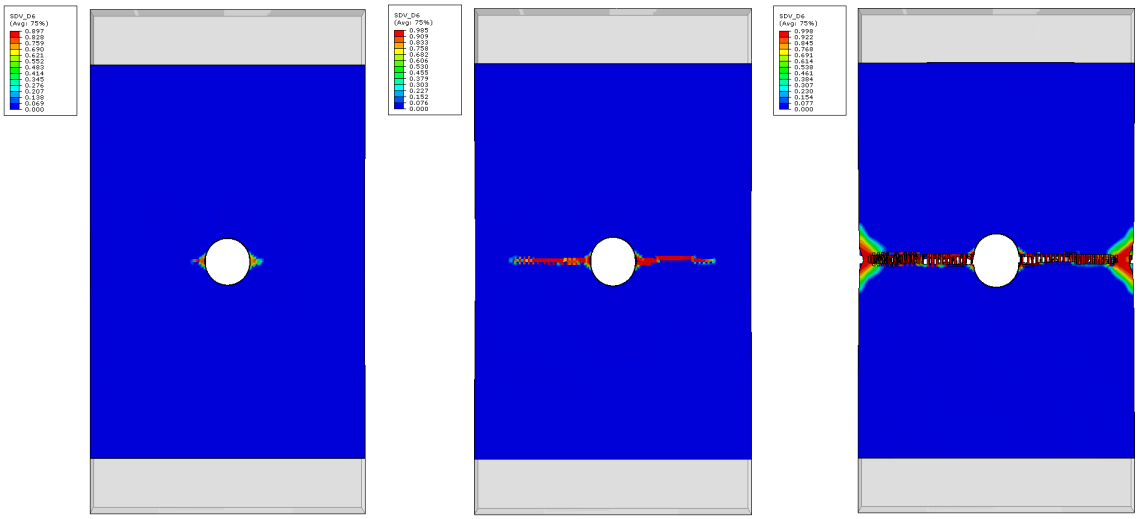

Figure 54: Evolution of the damage variable d_6 on the coupon OHT181. Translucency: On.

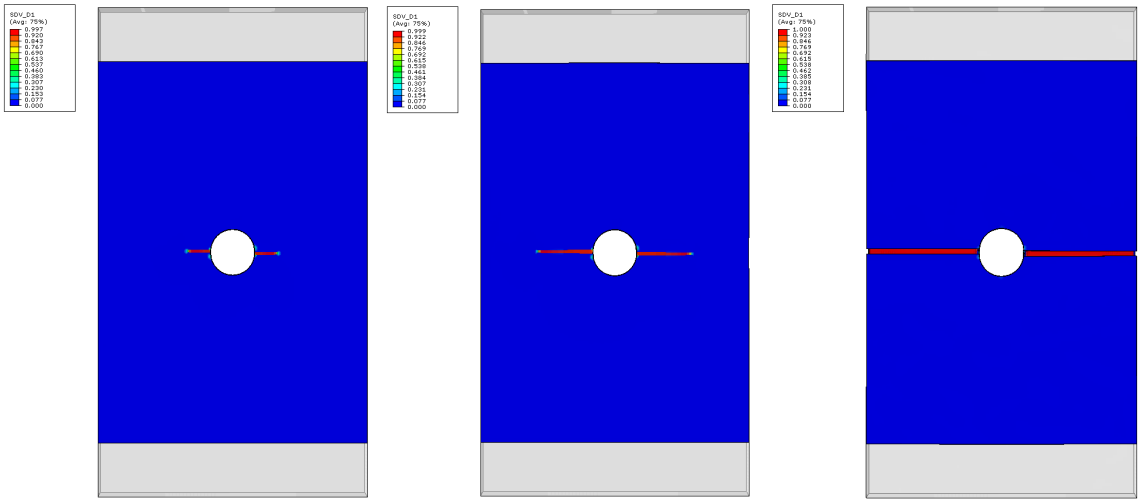

Figure 55: Evolution of the damage variable d_1 on the coupon OHT424. Translucency: On.

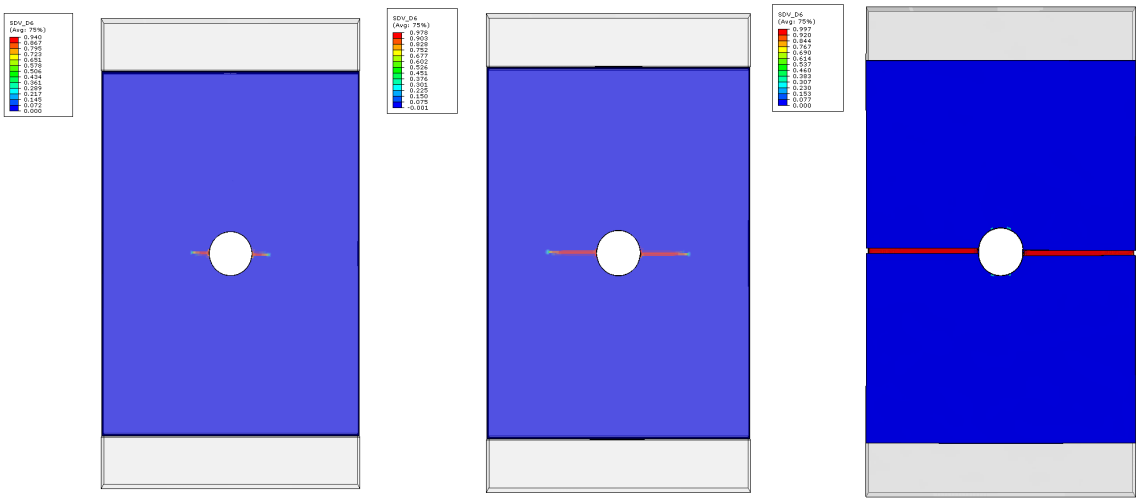

Figure 56: Evolution of the damage variable d_6 on the coupon OHT424. Translucency: On.